Supplementary Material

*for*

# Spatiotemporal properties of seismicity and variations of shear-wave splitting parameters in the Western Gulf of Corinth (Greece).

**Vasilis Kapetanidis[1], Georgios Michas[1], George Kaviris[1] and Filippos Vallianatos[1,2]**

1 Section of Geophysics – Geothermics, Department of Geology and Geoenvironment, National and Kapodistrian University of Athens, 15784 Panepistimiopolis, Athens, Greece; vkapetan@geol.uoa.gr (V.K.); gemichas@geol.uoa.gr (G.M.); gkaviris@geol.uoa.gr (G.K.); fvallian@geol.uoa.gr (F.V.)

2 Institute of Physics of Earth's Interior and Geohazards, UNESCO Chair on Solid Earth Physics and Geohazards Risk Reduction, Hellenic Mediterranean University Research Center, Grete, Greece

## Table of Contents

## Section S1: Location/Relocation statistics for Catalogue 1

Table S1 shows mean or median values of RMS travel-time residuals, azimuthal gap, horizontal (ERH) and vertical (ERZ) uncertainties of the absolute locations derived with the HypoInverse code (Klein, 2002) per spatial group, as well as for the whole Catalogue 1, regarding the 8,944 events that were successfully relocated (see also Michas et al., 2021). For reference to group numbers and colours, see Figure 2. Miscellaneous seismicity, at the margins of the study area or deeper than 15 km, has been classified into group #10. The median RMS error for the catalogue is 0.13 sec, which was also set as the value considered for the average arrival-time reading error that is taken into account for the calculation of location uncertainties. Other statistics for Catalogue 1 are presented in the form of histograms in Figure S1. The azimuthal gap is generally smaller than 150°, which is partly due to the incorporation of data from the regional HUSN stations. This is particularly useful for events near the margins of the local network, e.g. the westernmost part of group #4, whose hypocenters would otherwise be significantly more scattered. On the other hand, as discussed in the main text, this also causes some biases to the focal depths, leading to deeper hypocenters, which is not reflected by the nominal ERZ values reported by HypoInverse.

**Table S1.** Absolute location error and other statistics per spatial group (see Figure 2) for the seismicity of 2013–2014 (Catalogue 1) in the Western Gulf of Corinth (WGoC). Table after Michas et al. (2021).

| CLID | 1 | 2 | 3 | 4 | 5 | 6 | 7 | 8 | 9 | 10 | All |
|---|---|---|---|---|---|---|---|---|---|---|---|
| Colour | black | magenta | cyan | green | orange | red | yellow | brown | blue | gray | - |
| Region | S of Galaxidi | Eratini / Galaxidi | Itea | offshore Nafpaktos | Nafpaktos | offshore Aigion | Marathias | offshore Kamarai | Helike 2013 | margins/ deeper events | WGoC |
| # of events | 101 | 305 | 392 | 2025 | 549 | 1258 | 517 | 979 | 1832 | 986 | 8944 |
| Mean RMS (s) | 0.17 | 0.14 | 0.15 | 0.13 | 0.13 | 0.13 | 0.13 | 0.13 | 0.14 | 0.15 | 0.14 |
| Median RMS (s) | 0.16 | 0.13 | 0.13 | 0.12 | 0.12 | 0.12 | 0.12 | 0.13 | 0.13 | 0.13 | 0.13 |
| Mean Gap (°) | 102 | 109 | 100 | 98 | 91 | 94 | 76 | 73 | 93 | 98 | 92 |
| Mean ERH (km) | 0.41 | 0.43 | 0.44 | 0.34 | 0.34 | 0.34 | 0.30 | 0.32 | 0.32 | 0.44 | 0.35 |
| Median ERH (km) | 0.38 | 0.40 | 0.39 | 0.31 | 0.31 | 0.31 | 0.26 | 0.29 | 0.28 | 0.39 | 0.31 |
| Mean ERZ (km) | 1.68 | 0.97 | 0.95 | 0.77 | 0.57 | 0.58 | 0.55 | 0.64 | 0.41 | 1.56 | 0.74 |
| Median ERZ (km) | 1.15 | 0.73 | 0.67 | 0.59 | 0.48 | 0.51 | 0.47 | 0.59 | 0.33 | 1.09 | 0.55 |

Concerning the double-difference relocation procedure with HypoDD, as it was performed with weighted least-squares inversion using the conjugate gradients method, the reported relative location uncertainties are not meaningful (Waldhauser, 2001). To acquire a better estimate for the robustness of the relocation, we implemented a station jack-knife test using the same parameterization and grouping as for the actual relocation. For this test, the procedure was repeated by removing one station at a time. Then for each event, the distribution of its relocated hypocenter for each run of the jack-knife test was taken into account and the perturbations relative to its normal relocated position (without any stations removed) were calculated. Table S2 presents the statistics of these perturbations per spatial group. The mean or median absolute dx, dy are not larger than 52 m; horizontal perturbations dh (square root of $dx^2+dy^2$) are on average 50-82 m, while the respective average absolute dz values reach up to ~137 m. The standard deviations of the perturbation clouds of points show values ranging 75-139 m for horizontal and 97-351 m for vertical relative locations. The map of Figure S2 shows the 95% confidence interval ellipses for the horizontal perturbations of each event, yielded from the station jack-knife test. This shows that the relocation procedure is robust for the majority of events, with only few being unstable, likely due to the smaller number of available phases, which renders their solution more easily affected by the removal of a station. The same is true for focal depth perturbations, which are generally larger than the horizontal ones for most events (Figure S3).

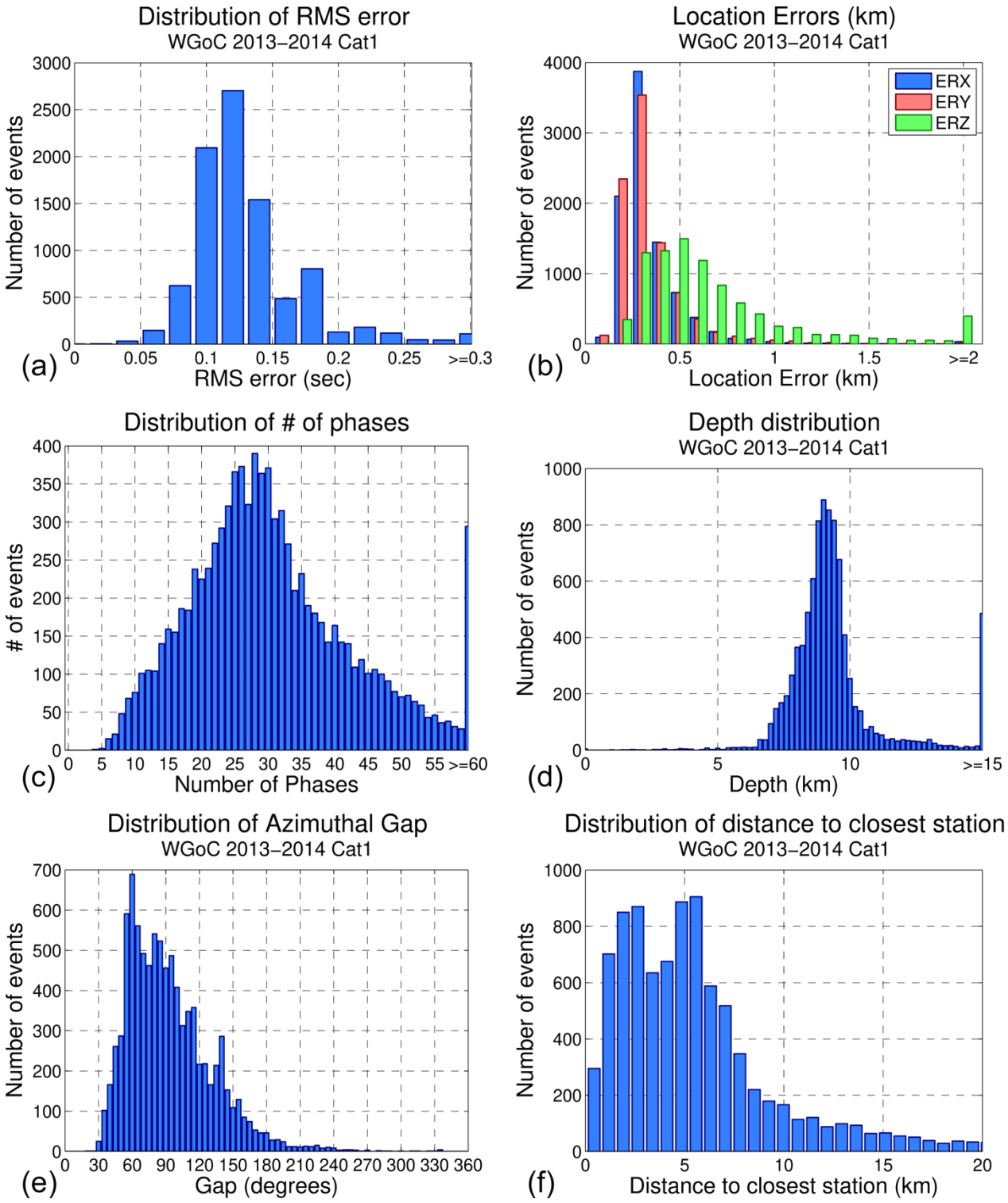


**Figure S1**. Location statistics for Catalogue 1. (a) RMS travel-time error, (b) horizontal (ERX, ERY) and vertical (ERZ) location uncertainties, taking into account an average arrival-time reading error of 0.13sec, (c) number of phases with non-zero true weight, (d) focal depth (including relocated hypocenters with HypoDD), (e) azimuthal gap and (f) epicentral distance of the nearest station with arrival-time data. Absolute location errors and RMS travel-time errors are nominal values reported by HypoInverse.

**Table S2.** Statistics of the station jack-knife test for the relocation robustness per spatial group of the 2013-2014 seismicity in the WGoC, with dx, dy and dz values representing perturbations from the true relocated hypocenter. The 95% confidence interval ellipse major semi-axis length refers to the horizontal ellipses of Figure S2, as estimated for each whole spatial group.

| **CLID** | **1** | **2** | **3** | **4** | **5** | **6** | **7** | **8** | **9** | **10** |
|---|---|---|---|---|---|---|---|---|---|---|
| **Colour** | **black** | **magenta** | **cyan** | **green** | **orange** | **red** | **yellow** | **brown** | **blue** | **gray** |
| **Region** | S of Galaxidi | Eratini / Galaxidi | Itea | offshore Nafpaktos | Nafpaktos | offshore Aigion | Marathias | offshore Kamarai | Helike 2013 | margins/ deeper events |
| **mean abs. dx** (m) | 37.4 | 42.2 | 39.9 | 50.7 | 32.1 | 42.6 | 26.8 | 33.9 | 39.7 | 52.1 |
| **mean abs. dy** (m) | 36.2 | 41.3 | 38.4 | 51.3 | 31.7 | 42.9 | 27.2 | 33.4 | 40.5 | 52.4 |
| **mean dh** (m) | 57.2 | 65.7 | 61.6 | 80.1 | 50.1 | 67.4 | 42.5 | 52.8 | 63.0 | 82.1 |
| **mean abs. dz** (m) | 137.6 | 88.3 | 63.8 | 105.3 | 48.5 | 67.4 | 39.8 | 48.2 | 58.3 | 124.7 |
| **median abs. dx** (m) | 11.6 | 11.6 | 9.6 | 20.0 | 10.6 | 14.5 | 8.6 | 10.3 | 17.0 | 21.6 |
| **median abs. dy** (m) | 10.9 | 11.1 | 10.0 | 20.1 | 10.2 | 14.8 | 8.6 | 10.5 | 17.3 | 21.4 |
| **median dh** (m) | 21.7 | 22.3 | 19.1 | 38.6 | 20.1 | 28.5 | 16.7 | 20.7 | 33.2 | 39.2 |
| **median abs. dz** (m) | 37.0 | 25.0 | 18.0 | 37.0 | 16.0 | 22.0 | 14.0 | 13.0 | 25.0 | 44.0 |
| **st.dev dx** (m) | 89.6 | 137.9 | 117.6 | 118.6 | 84.7 | 112.9 | 75.3 | 98.7 | 84.9 | 128.8 |
| **st.dev dy** (m) | 92.2 | 123.0 | 100.1 | 122.3 | 83.0 | 110.3 | 75.7 | 93.4 | 88.8 | 139.2 |
| **st.dev dz** (m) | 348.3 | 253.0 | 158.7 | 280.5 | 139.7 | 165.4 | 97.4 | 136.5 | 183.9 | 350.7 |
| **95% c.i. ellipse major semi-axis** (m) | 230.9 | 341.8 | 289.8 | 306.9 | 209.1 | 277.6 | 190.4 | 244.2 | 218.9 | 340.6 |

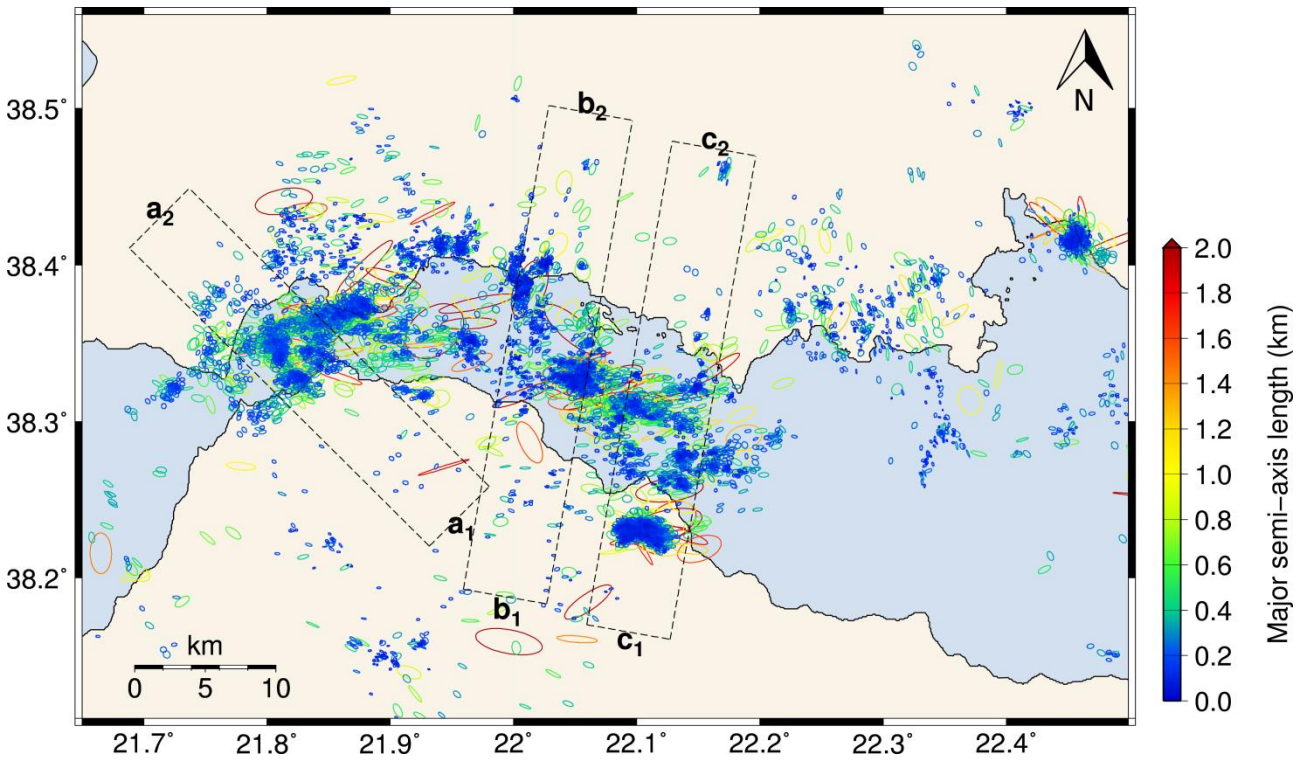


**Figure S2**. Distribution of 95% c.i. ellipses for epicentral perturbations derived by the station jack-knife test for the robustness of the relocation procedure.

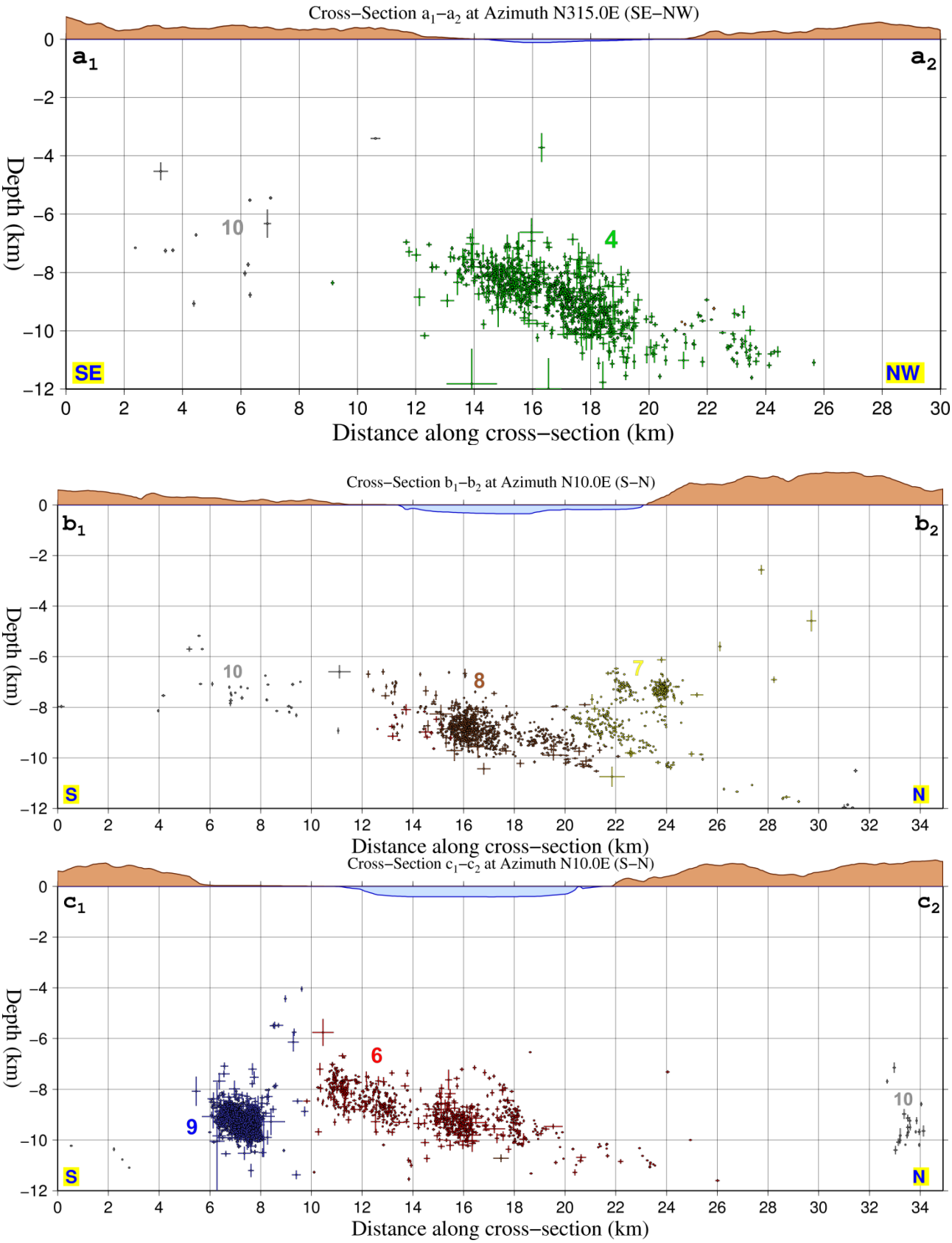


**Figure S3**. Cross-sections $a_1$-$a_2$ to $c_1$-$c_2$ (Figure S2) with vertical and horizontal bars representing the vertical and horizontal (square root of $dx^2+dy^2$) average perturbation of each hypocenter, respectively, derived by the application of the station jack-knife test for the robustness of the relocation procedure.

## Section S2: Seismic moment measurements

For the calculation of the seismic moment, we perform the procedure described by Kapetanidis (2017). For each available waveform with adequate signal-to-noise (SNR) ratio, the signal is de-trended, high-pass-filtered above 0.3 Hz and the S-wave window is cropped. Fast Fourier Transform is calculated, the signal is converted into velocity, by removing the instrument's response, then integrated into displacement and finally converted to seismic moment units via the following formula (Boatwright, 1978; Bowers and Hudson, 1999):

$$M(f) \approx \frac{4\pi\rho\beta^3}{F_{RMS}R_S}\frac{R}{S_S}\Psi(f) \quad \text{(S1)}$$

with $\Psi(f)$ the displacement spectrum, $\rho$ the material's density, $\beta$ the shear-wave velocity, $R$ the hypocentral distance, $F_{RMS}$=0.63 the root mean square average of the radiation pattern for S-waves (Aki and Richards, 2002; Boore and Boatwright, 1984), $R_S$=2 the free surface correction and $S_S$ a station-dependent site-effect correction, initially set to 1. Similarly, a noise window is cropped before the arrival of the P-waves and its spectrum is converted to seismic moment units. We then fit the source model of Boatwright (1978) to the seismic moment spectrum through a least-squares inversion procedure, using the spectral SNR (dividing the respective signal to noise spectral amplitudes for common frequencies) as weight. The most important parameter of the fit is the seismic moment $M_o$, which corresponds to the plateau of spectral amplitudes at the lower frequencies. Then, the moment magnitude, $M_w$, is calculated using the formula of Hanks & Kanamori (1979):

$$M_w = \frac{2}{3}\left(\log_{10}\frac{M_o}{N\cdot m} - 9.1\right) \quad \text{(S2)}$$

The initial fit for the 15 July 2013, $M_w$=3.8, event is presented in Figure S4 (top) for a short-period station, where the plateau parameter, $M_o$, has been overestimated, as the spectral amplitudes keep increasing towards the lower frequencies.

To ameliorate the fit of the source model to the spectra, after a "first pass" of the above-mentioned procedure, the residuals between the fit model and spectral amplitudes are calculated for each station and component and then averaged for each frequency (Figure S5). This is performed for each epoch available in the stations metadata, so that different corrections are calculated for each epoch, in case instrumentation changes have been made during the study period. Systematic deviations between the calculated moment magnitudes at a station and the median $M_w$ values from all available stations are also taken into account, in case of problems with a certain station's response or with a particular component. Finally, a "second pass" of the spectral fitting procedure is performed, after the correction of spectral amplitude residuals and systematic offsets. Figure S4 (bottom) shows the result of spectral fitting after residual correction, where the signal at the lower frequencies is now more flat, permitting a better estimation of the plateau value, $M_o$. Likewise, Figure S6 shows another example for the same event with a broad-band station. In that case the correction is only minor (visually) but still manages to reduce a small overestimation of the $M_w$. A trimmed mean of the $M_w$ values calculated from all stations and components is registered as the final magnitude for each event. A similar procedure for the calculation of the seismic moment magnitude has been previously applied by Kapetanidis (2017) and Kapetanidis et al. (2015, 2020).

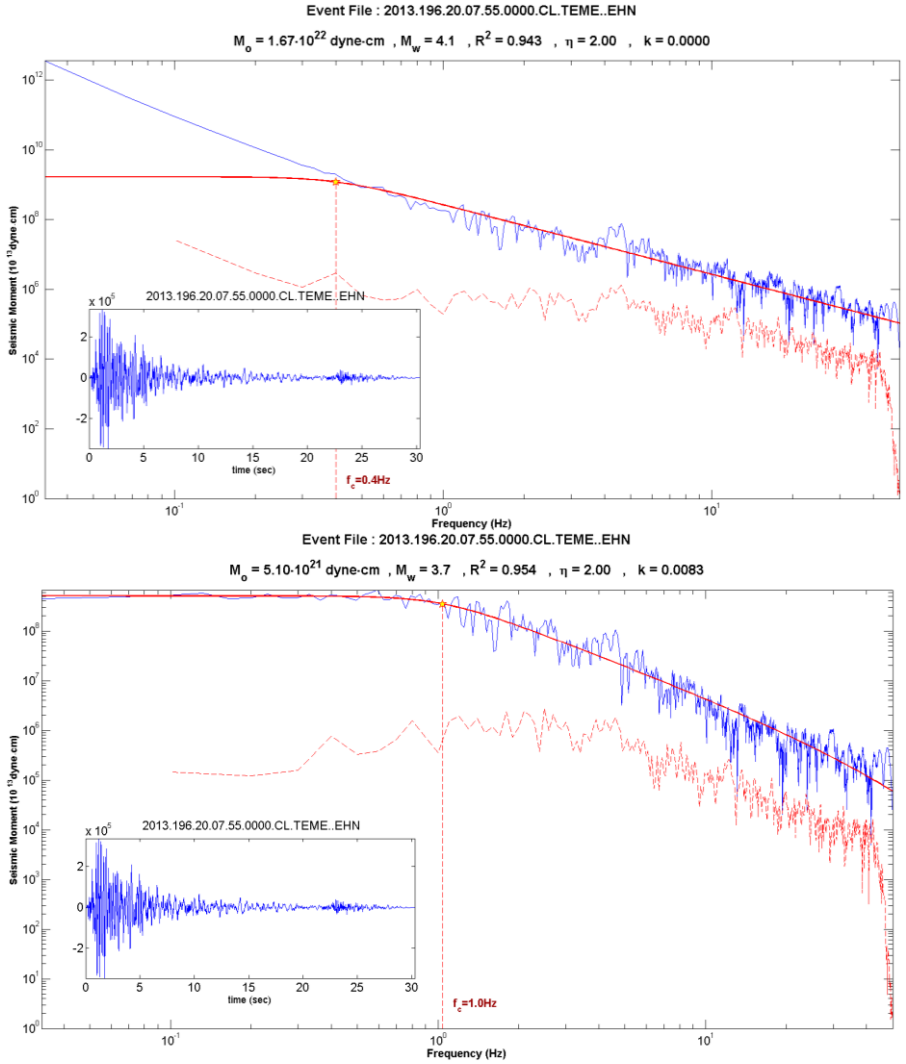


**Figure S4**. Example of seismic moment calculation by spectral fitting for the 15 July 2013, $M_w$=3.8 event on the short-period station TEME (top) before residual correction and (bottom) after residual correction. The blue and dashed red lines correspond to signal and noise spectra, respectively. The S-wave window is also presented in the inset panel at the bottom-left.

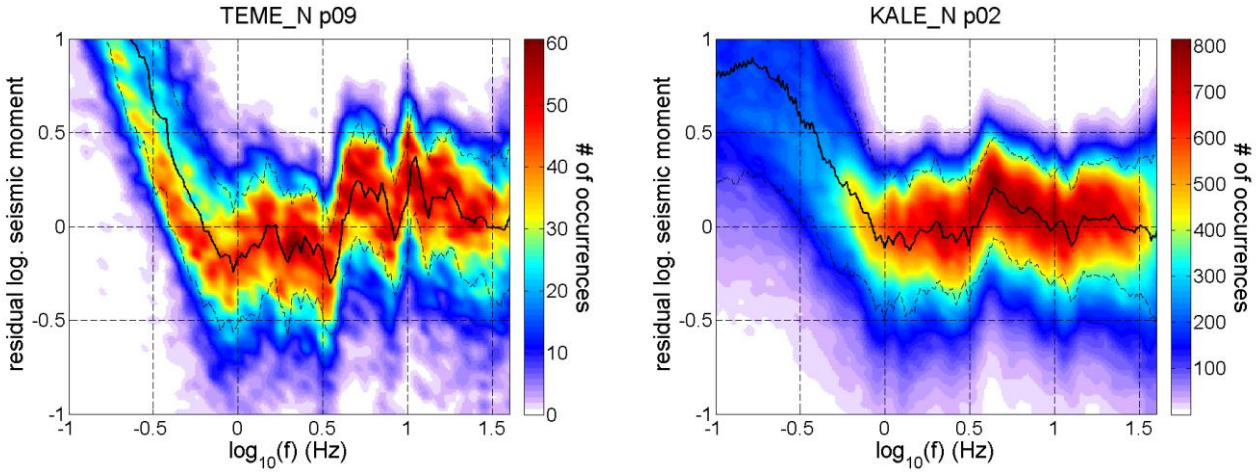


**Figure S5**. Examples of spectral moment fit residual distribution (left) for the short-period station TEME and (right) for the broad-band station KALE.

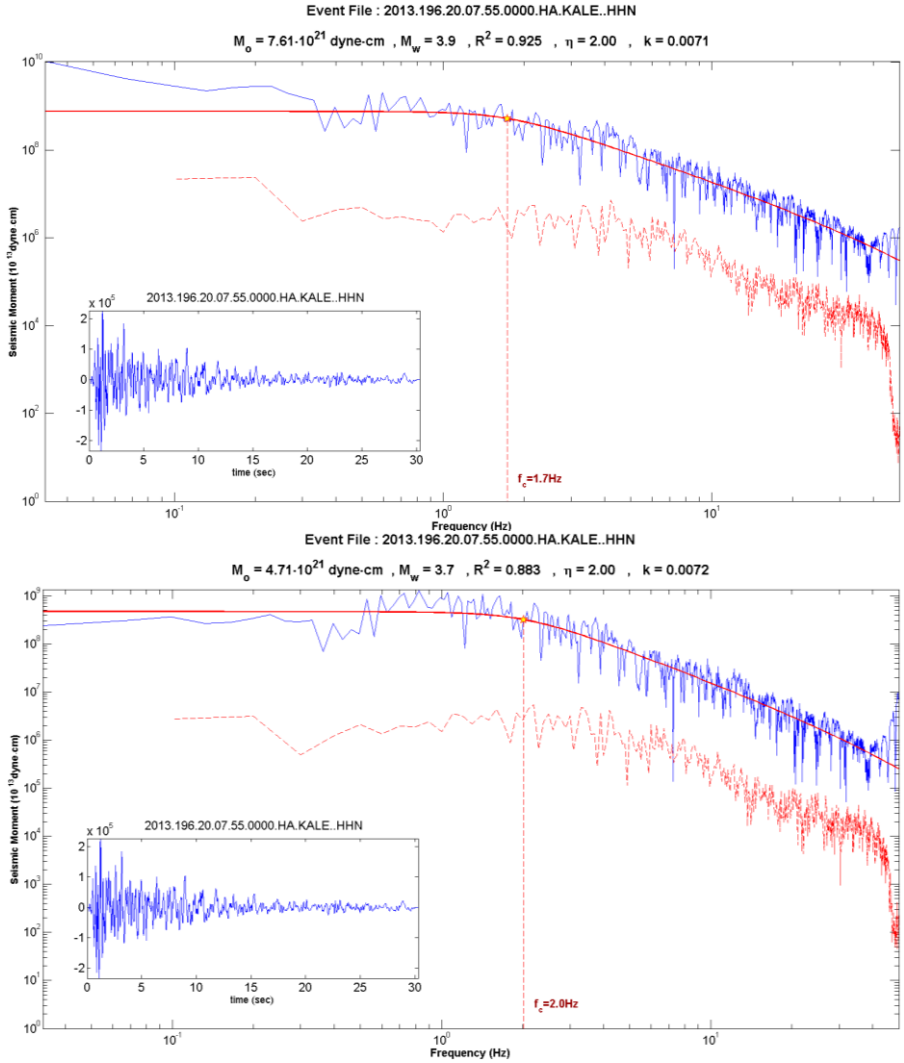


**Figure S6**. Same as Figure S4, but for the recording of the 15 July 2013, $M_w$=3.8 event on the broad-band station KALE (top) before residual correction and (bottom) after residual correction.

## Section S3: Automatic picking for Catalogue 2

Figure S7a shows the map of epicenters from the automatic catalogue of the Corinth Rift Laboratory (CRL; http://ephesite.ens.fr/~eworm/), with over 43,000 detected and located events during the period 2013-2014 in the region of the WGoC. Although a significant percentage of these locations is concentrated in the regions highlighted from the manual Catalogue 1 as being active with dense seismicity and swarms, the initial automatic catalogue contains events of regional seismicity outside the WGoC which were detected but mislocated. It also includes certain low quality locations, some of which can be visualized as cross-hair artifacts at specific latitudes and longitudes corresponding to the co-ordinates of certain stations. Herein, we use the available automatic detections available in this catalogue, remove regional events outside the area of study, select a subset of events with adequate SNR and attempt to improve their arrival-time picks to provide better locations.

Initially, events which were already available in Catalogue 1 were removed from the automatic catalogue. Then events' waveforms were plotted along with their automatic P and S picks, and very noisy recordings or signals belonging to regional events were removed by visual inspection. In many cases, especially during swarms or aftershock sequences, several events occur in the same region within seconds from one another. As a result, their waveforms overlap and are both hard to pick/locate and unusable for shear-wave splitting measurements; such events were also discarded. The rest of events were filtered using moderate RMS error and location uncertainty criteria, to remove grossly mislocated events.

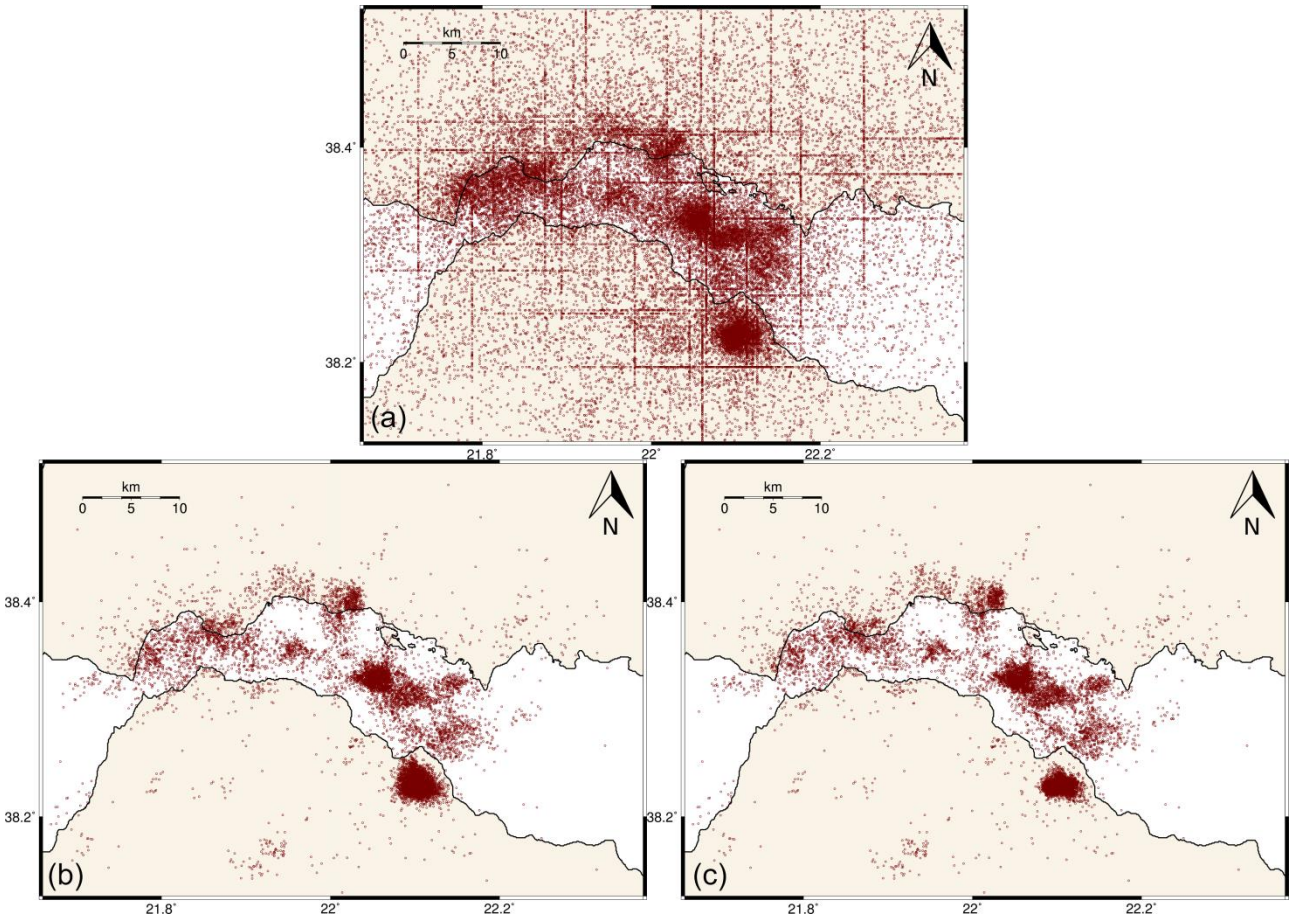


**Figure S7**. (a) Map of automatic CRL locations for 2013-2014. (b) Map of automatic locations for Catalogue 2 in this study, after removal of regional events/low quality locations and with the combined application of multiple-window AIC and template-matching picking methods and (c) same as (b), but after the removal of average travel-time residuals, as a rough application of station corrections for groups 4-9.

The remaining dataset was processed through two automatic picking methods for further validation, which are briefly presented herein. The first assumes that the noise and P-wave (or S-wave) signals are locally stationary and can be described by two auto-regressive (AR) models with different coefficients. The Akaike's Information Criterion (AIC; e.g. Akazawa, 2004) is used for the identification of the optimal point that divides these two different AR processes. We employ a procedure which applies AR-AIC over a series of windows with different lengths, centered on an approximate arrival-time pick, such as the one that was previously available (e.g. automatic picks from the CRL database) or a theoretically expected arrival-time, based on an initial location. AIC is calculated using the formula of Maeda (1985):

$$AIC(k) = k \cdot \log\{\mathrm{var}(x[1,k])\} + (N-k-1)\log\{\mathrm{var}(x[k+1,N])\} \quad \text{(S3)}$$

where $x$ is the filtered signal amplitude of a waveform segment with $N$ samples and var() is the variance for the range of samples within brackets, i.e. 1 to $k$ or $k$+1 to $N$, respectively. If the sample window contains part of noise and signal, the global minimum of AIC at $k = k_{min}$ should correspond to the wave onset, i.e. the point that best divides the two AR models. By applying this calculation in multiple windows centered on the vicinity of a probable wave onset, we examine whether the AIC minima are similar for most windows or scattered in a wide range of arrival-time values. Both the scattering and the amplitude of the AIC minima are taken into account to determine the arrival-time and its quality.

Figure S8 shows an example of an automatic pick using the abovementioned method for a P-wave arrival at station AIOA. A strong AIC minimum is calculated for the Z component, while all minima are well-constrained. Figure S9 is an example of the method's application on an S-wave arrival. The AIC functions are broader, as the onset is less discernable under the presence of the P-coda wave-train and the possible onset of other phases that arrive before the S-wave (e.g. minima on the E-W component at an earlier time). Finally, a very noisy arrival is presented in Figure S10, where the algorithm rejected the pick due to the significant scattering and low amplitude of the AIC minima. More details on the procedure are described by Kapetanidis (2017).

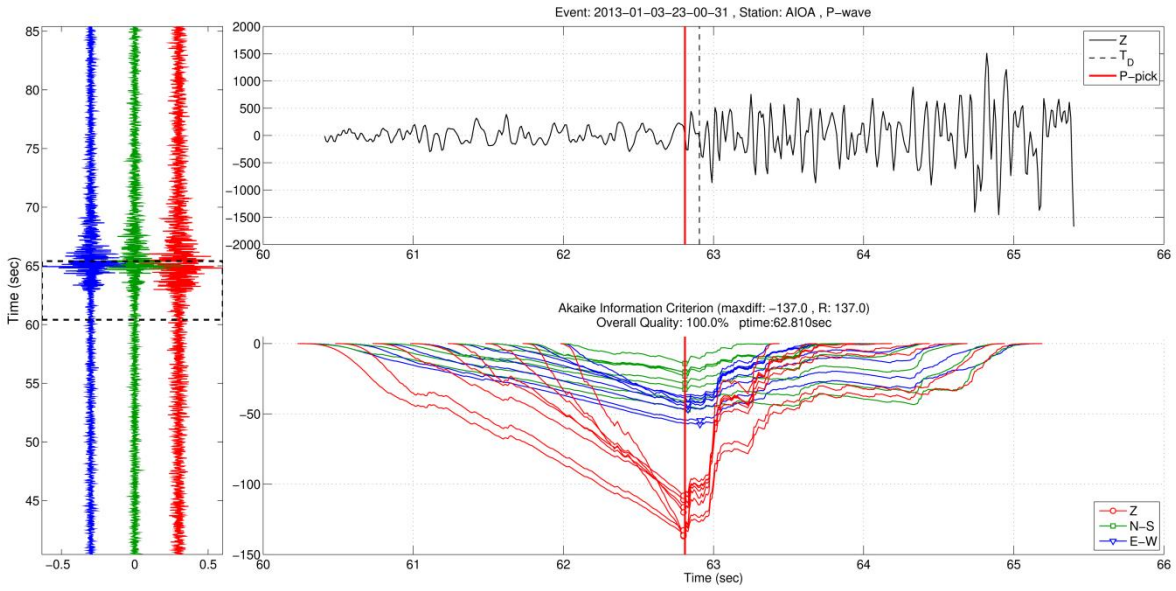


**Figure S8**. Example of an automatic pick on the P-wave using the multiple-window AR-AIC method. (Top) The Z component in the maximum length window, along with the approximate arrival (dashed black line) and the final pick on the P-wave (red). (Bottom) AIC function for different components (red=Z, green=N-S, blue=E-W) calculated in multiple different window lengths. For this visualization, the maximum of the AIC functions has been subtracted and their values are normalized in proportion to the window length. (Left) Waveform windows for the three components, with the same colours as in the bottom panel. The dashed rectangle shows the maximum length window (top panel).

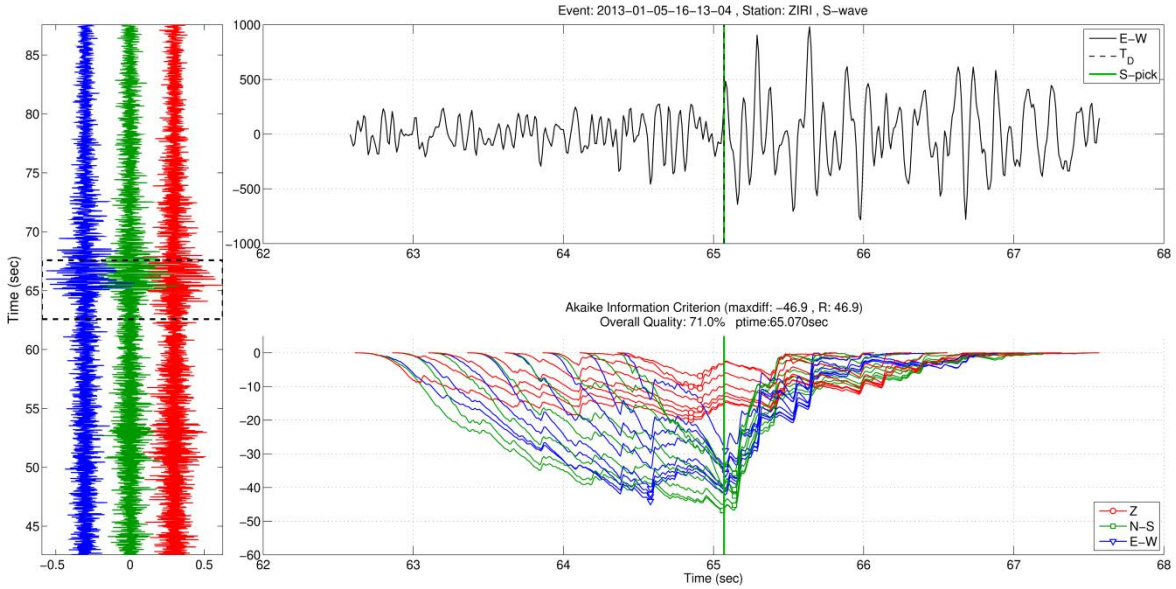


**Figure S9**. Same as Figure S8, but for an automatic pick on an S-wave.

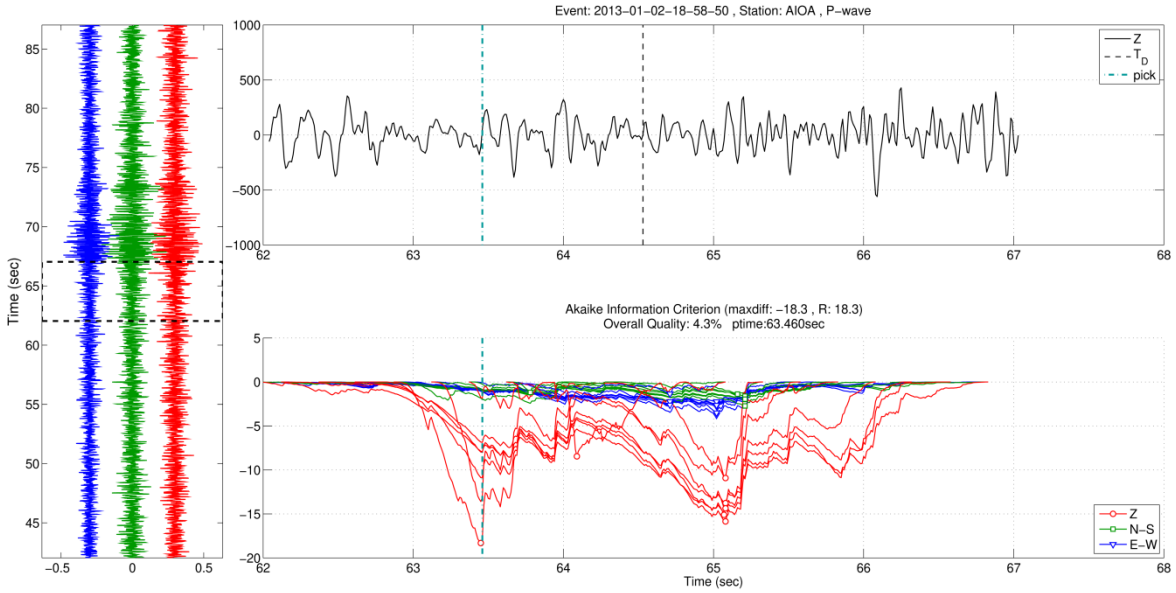


**Figure S10**. Example of a rejected automatic pick due to excess noise resulting in scattered AIC minima.

The second method that we have employed involves a template matching, or correlation detector technique (e.g. Schaff & Waldhauser, 2005). We use the available manual picks from Catalogue 1 to create a database of template waveforms, i.e. P- and S-wave windows for each station. Then, for each automatically detected event in Catalogue 2, we examine the respective recordings at each station (target waveform) and use the template waveforms as correlation detectors. Each template slides along the target waveform and the correlation coefficient is measured for each time-lag. The global maximum of the correlation coefficient indicates the position where the template best fits the common segment of the target waveform. At this point, the relative position of the respective P- or S-wave pick on the template can be transferred to the target and considered as a candidate P or S arrival-time pick, depending on the type of template. This is performed for a large number of templates on each target waveform and multiple measurements are acquired, each with its own correlation coefficient maximum. This procedure manages to pick P- and S-waves of events which are strongly correlated to those of the manual catalogue. Two examples are presented in Figures S11 and S12. The final P- or S-wave pick, marked on top of the target

waveform, is calculated as a weighted mean of the individual picks, using the respective correlation coefficient maximum (CC) values as weights. Similar template-matching techniques have been described in detail and applied by Kapetanidis & Papadimitriou (2011) and Kapetanidis (2017).

After the application of the above-mentioned automatic picking methods, new hypocentral solutions were derived by Hypoinverse and further assessed for their quality (Figure S7b). The last stage in the processing of Catalogue 2 involved the removal of average P- and S-wave travel-time residuals as an application of roughly determined station-corrections, applied separately on groups 4-8 and 9, which slightly enhanced the image of their epicentral distribution (Figure S7c).

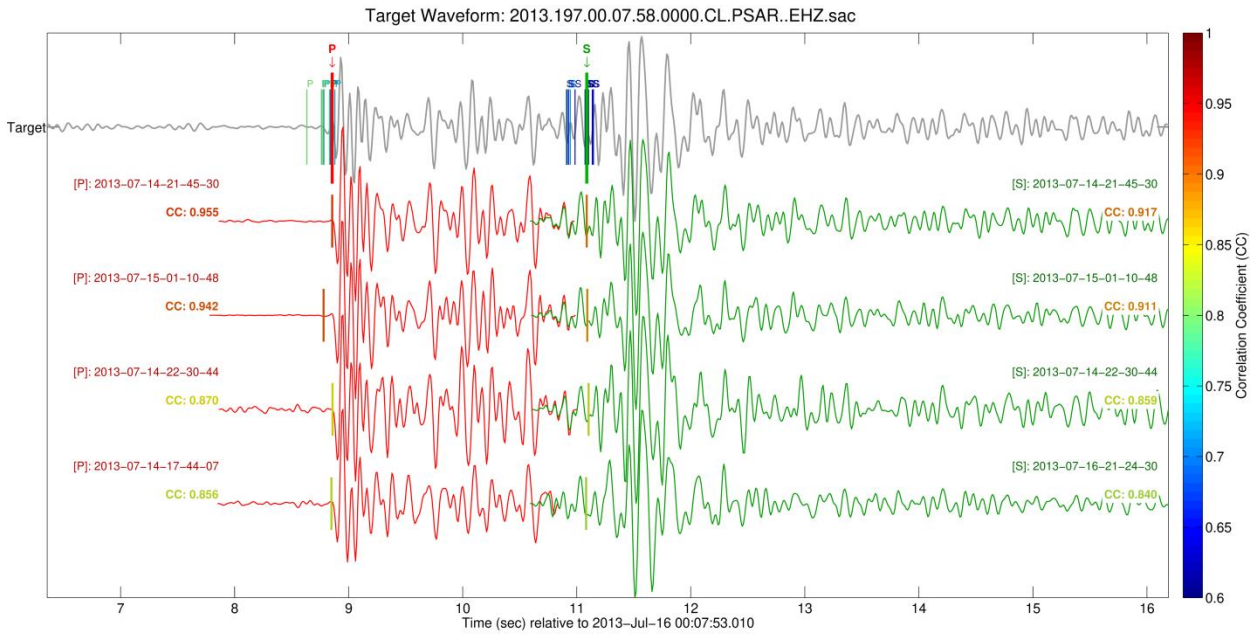


**Figure S11**. Example of automatic picks on P- and S-waves using the template matching method. The top waveform (black) belongs to the target event (to be picked). Red and green waveforms correspond to the best matching P- and S-wave templates, respectively. Arrival-time picks shown as vertical lines on the templates, with their colour corresponding to their correlation coefficient (CC). The final P- and S-wave pick is marked on the target waveform with a down-pointing arrow at the top of a red and green thick line, respectively. Available picks from more templates (with lower CC) are also shown on the target waveform.

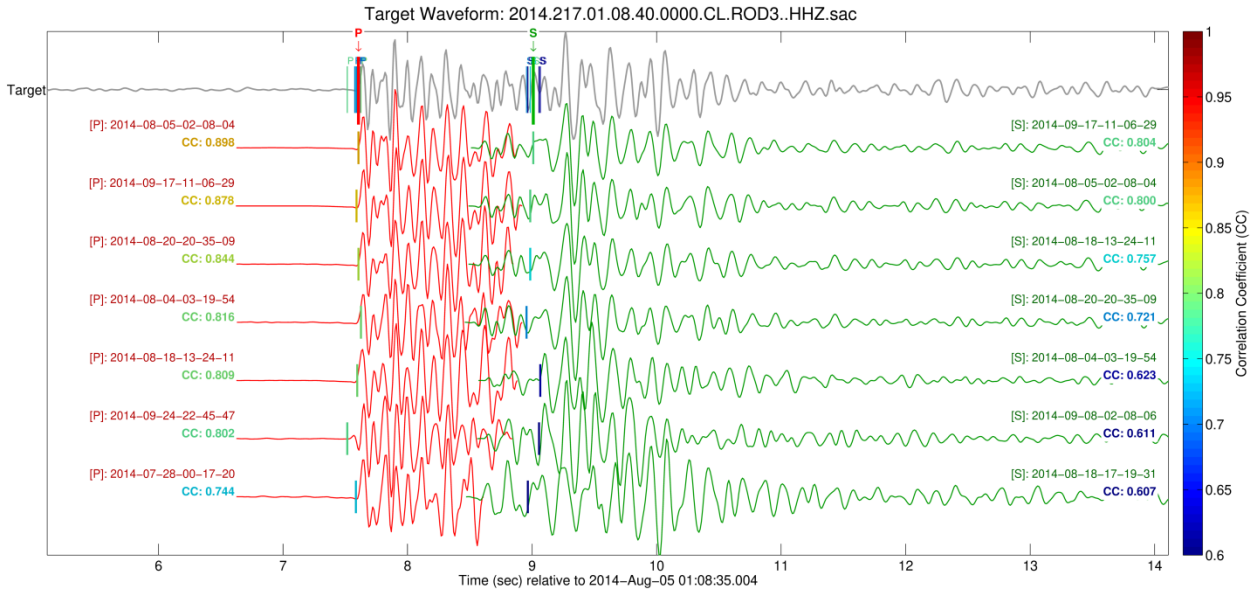


**Figure S12**. Same as Figure S11, but for a different target waveform.

## Section S4: Additional tables and figures

**Table S3:** Mean values of SWS parameters and their respective errors per station for valid measurements (grade A-C) of Catalogue 3. Stations with additional data from Catalogue 2 are marked with a star (*) next to their station code. Errors $\delta\bar{\varphi}$ correspond to the 95% c.i, whereas $\delta\bar{t_d}$ and $\delta\bar{t_n}$ are the typical error of mean. *N* is the number of valid measurements per station. The first line in bold corresponds to all valid measurements of Cat3.

| Station | N | $\bar{\varphi}$ (°) | $\delta\bar{\varphi}$ (°) | $\bar{t_d}$ (ms) | $\delta\bar{t_d}$ (ms) | $\bar{t_n}$ (ms/km) | $\delta\bar{t_n}$ (ms/km) |
|---|---|---|---|---|---|---|---|
| **ALL*** | **4476** | **103.2** | **1.9** | **118.5** | **0.9** | **9.6** | **0.1** |
| AGRP* | 60 | 97.1 | 9.6 | 92.7 | 8.1 | 6.5 | 0.6 |
| AIOA* | 248 | 82.8 | 6.2 | 74.0 | 3.1 | 5.8 | 0.2 |
| ALIK* | 542 | 115.9 | 5.7 | 135.1 | 2.6 | 13.1 | 0.3 |
| EFP | 72 | 82.4 | 11.5 | 122.1 | 8.1 | 9.8 | 0.7 |
| HELI | 56 | 77.6 | 11.6 | 71.3 | 4.5 | 7.4 | 0.5 |
| KALE* | 249 | 127.7 | 7.6 | 101.7 | 3.6 | 7.3 | 0.3 |
| LAKA* | 264 | 133.8 | 4.2 | 122.8 | 3.2 | 8.5 | 0.2 |
| MALA* | 80 | 69.7 | 10.2 | 118.5 | 5.8 | 10.3 | 0.5 |
| MG00 | 45 | 82.2 | 7.5 | 126.2 | 9.0 | 10.4 | 0.8 |
| MG02 | 88 | 94.1 | 12.3 | 111.3 | 7.2 | 9.8 | 0.7 |
| MG03 | 44 | 67.1 | 30.8 | 111.8 | 9.3 | 9.2 | 0.7 |
| MG04 | 68 | 106.3 | 19.8 | 113.8 | 7.3 | 9.6 | 0.6 |
| MG05 | 29 | 60.7 | 26.3 | 107.6 | 10.1 | 9.1 | 1.1 |
| MG06* | 185 | 86.6 | 6.3 | 126.3 | 4.4 | 10.2 | 0.4 |
| MG07 | 70 | 96.3 | 26.9 | 113.9 | 7.7 | 9.8 | 0.7 |
| PANR | 17 | 132.8 | 36.6 | 105.3 | 14.1 | 7.2 | 0.9 |
| PSAM* | 53 | 93.1 | 8.9 | 91.9 | 7.9 | 7.5 | 0.7 |
| PSAR* | 741 | 95.0 | 2.8 | 144.7 | 2.4 | 10.1 | 0.2 |
| PYRG* | 350 | 102.4 | 29.6 | 116.3 | 3.2 | 9.8 | 0.3 |
| ROD3* | 231 | 110.3 | 8.2 | 123.9 | 4.0 | 9.8 | 0.3 |
| SERG | 87 | 58.4 | 7.5 | 86.0 | 6.1 | 6.6 | 0.5 |
| TEME* | 244 | 139.7 | 5.2 | 119.2 | 3.3 | 12.4 | 0.4 |
| TRIZ* | 236 | 93.4 | 5.4 | 105.4 | 3.6 | 9.0 | 0.3 |
| VVK | 27 | 115.2 | 23.8 | 85.2 | 12.7 | 6.9 | 1.0 |
| ZIRI* | 390 | 110.2 | 5.2 | 112.1 | 3.1 | 8.6 | 0.2 |

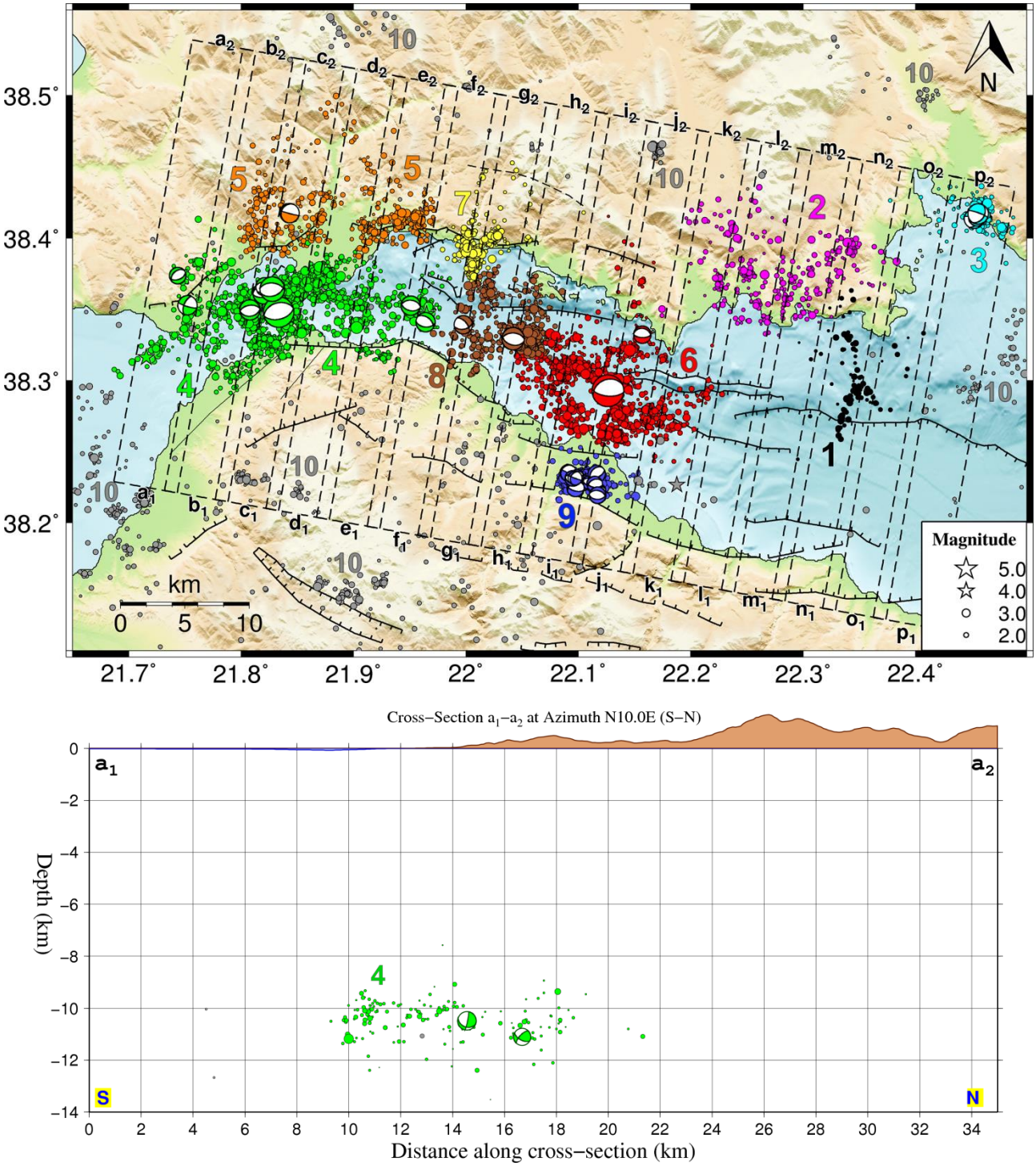


**Figure S13**. (Top) Map of relocated seismicity for 2013-2014 in the WGoC. Colours correspond to the 9 spatial groups in which the dataset was divided, along with the "miscellaneous" group #10 (gray). Beachballs depict the focal mechanisms of major events (Table 1). (Bottom panels) Vertical cross-sections $a_1$-$a_2$ to $p_1$-$p_2$, drawn in a N10°E direction, corresponding to the dashed rectangles shown on the map (top). Beachballs depict the far hemisphere projections of focal mechanisms for major events. Black dashed lines at the top of the cross-sections indicate the position of mapped active faults with inferred extension at a 60° dip. For mapped faults' names refer to Figure 1.

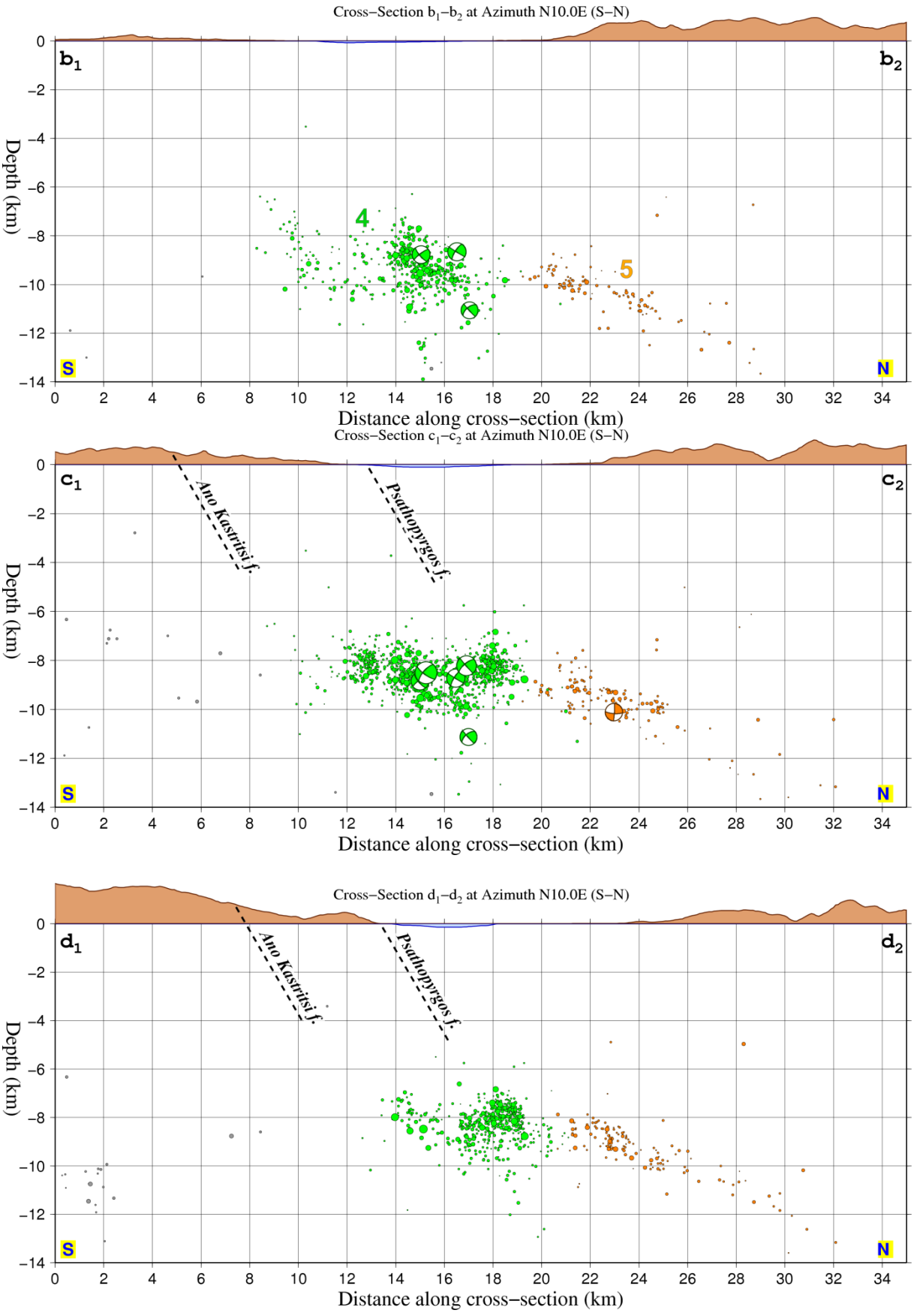


**Figure S13:** (continued)

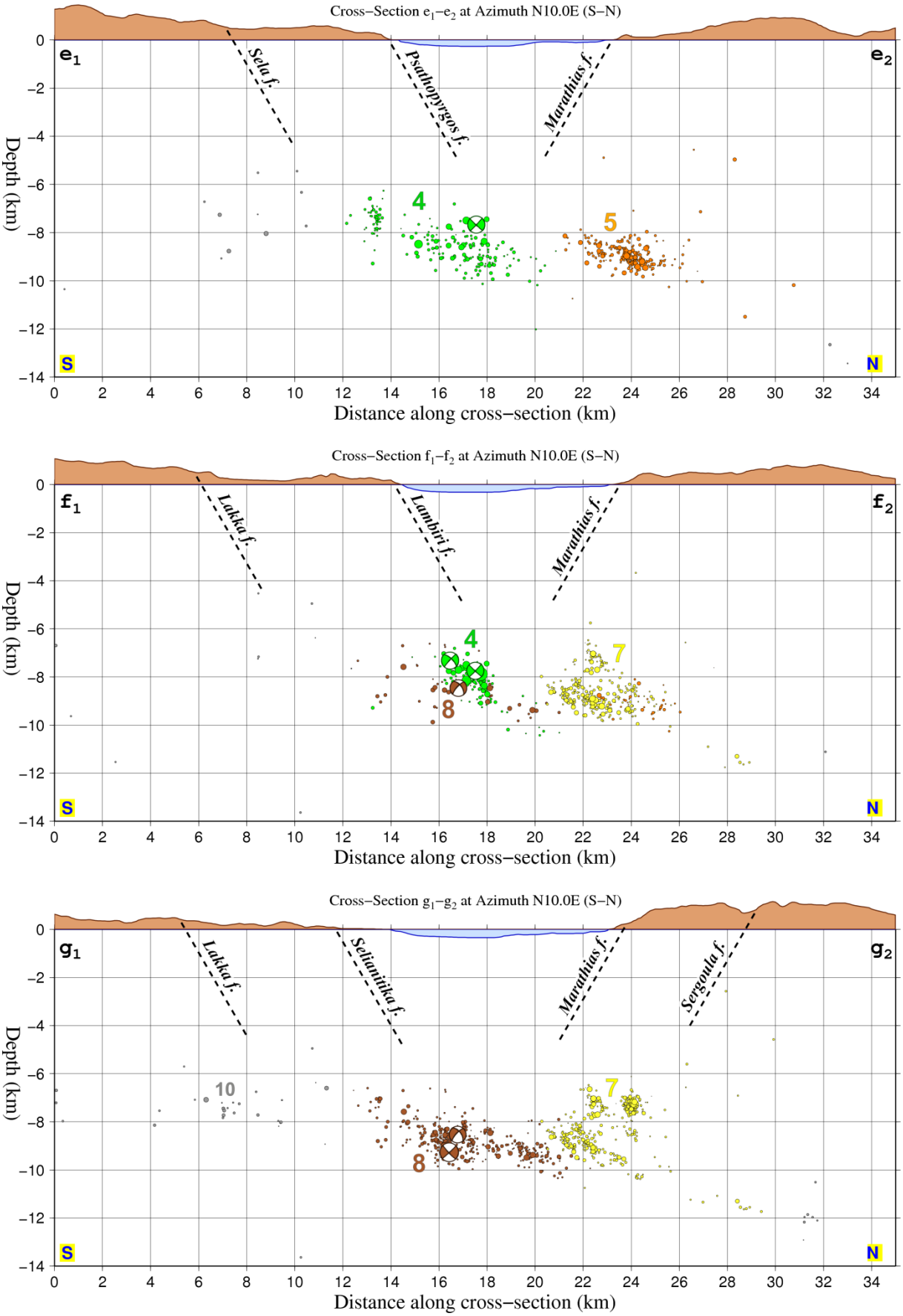


**Figure S13:** (continued)

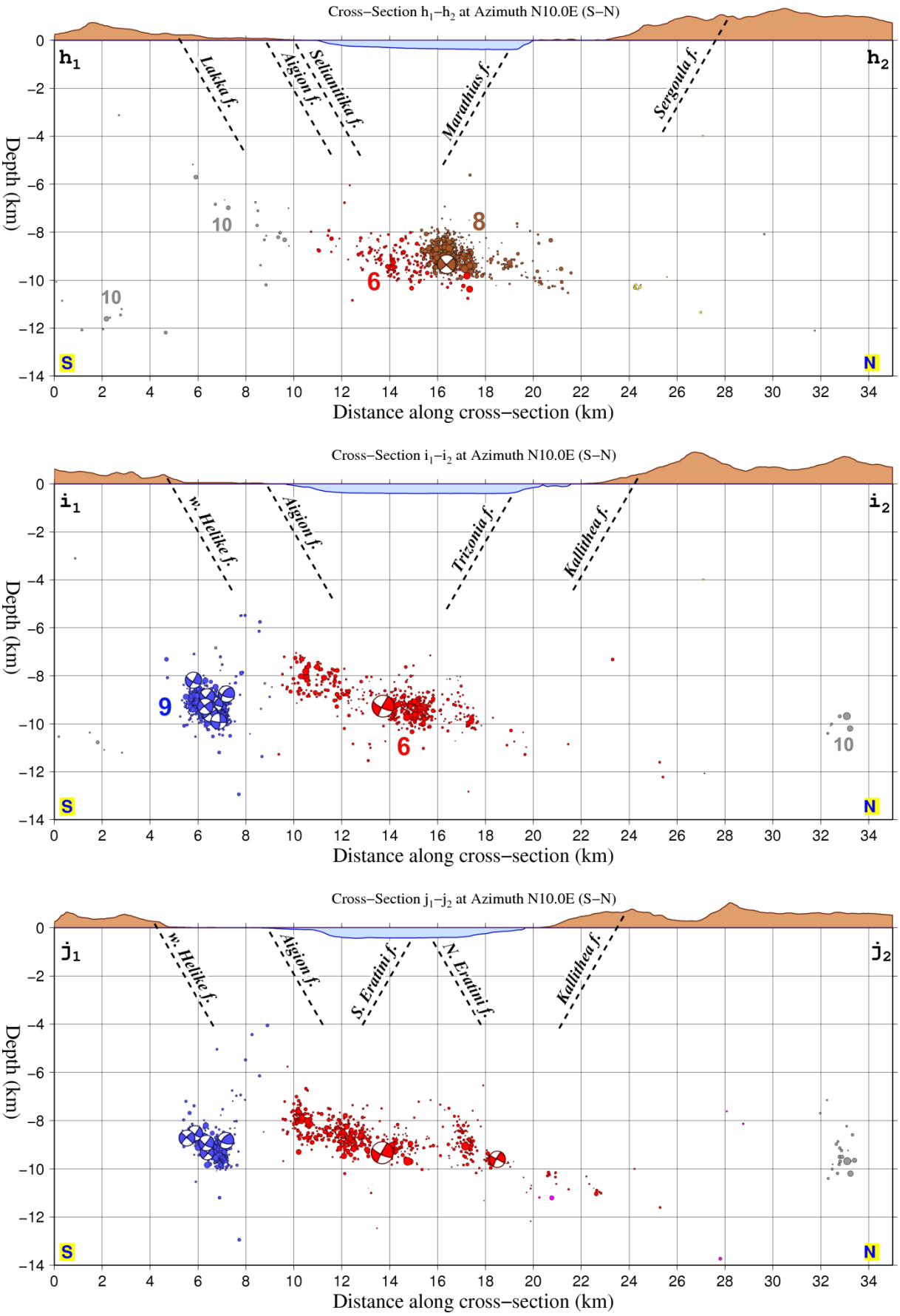


**Figure S13:** (continued)

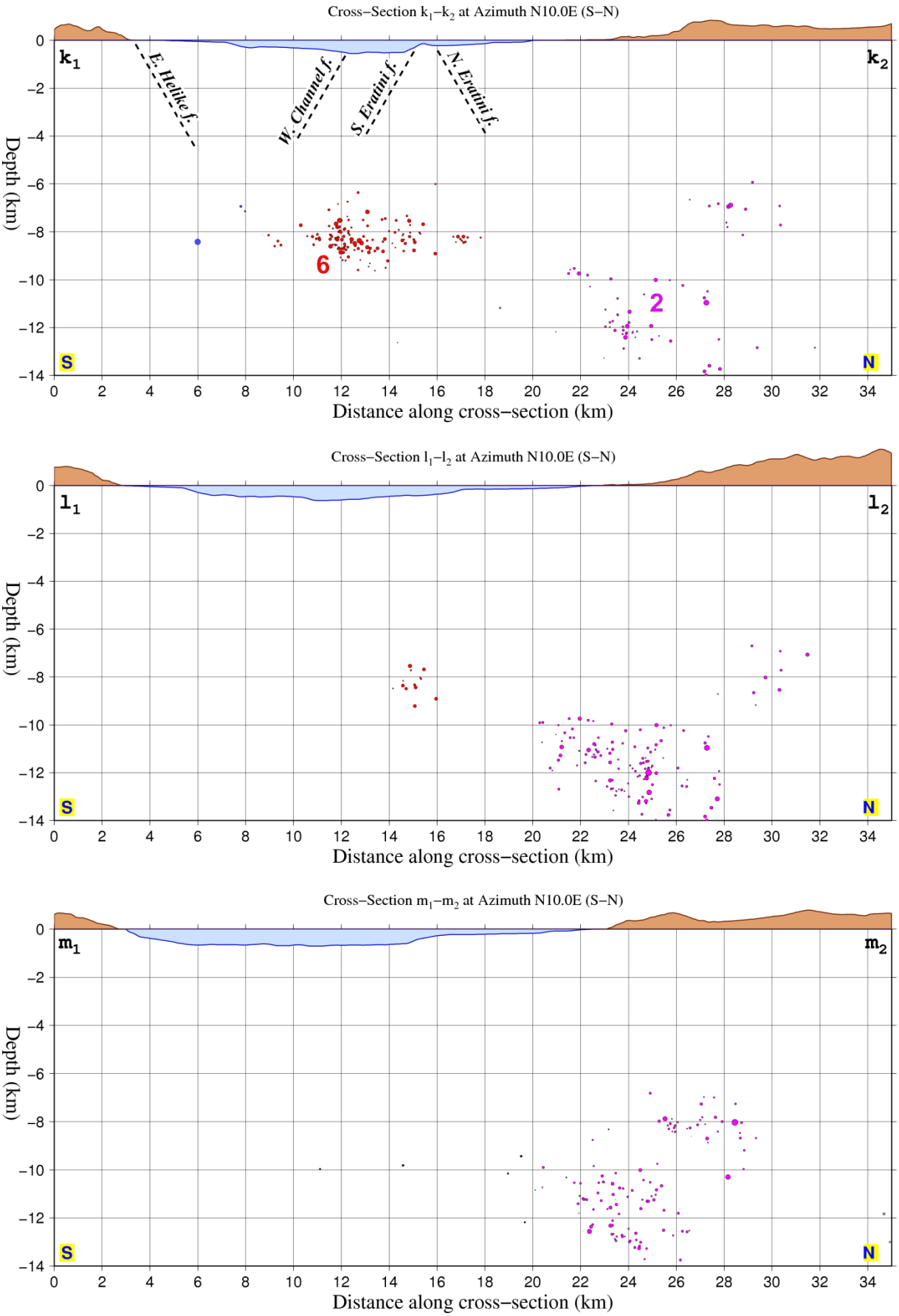


**Figure S13:** (continued)

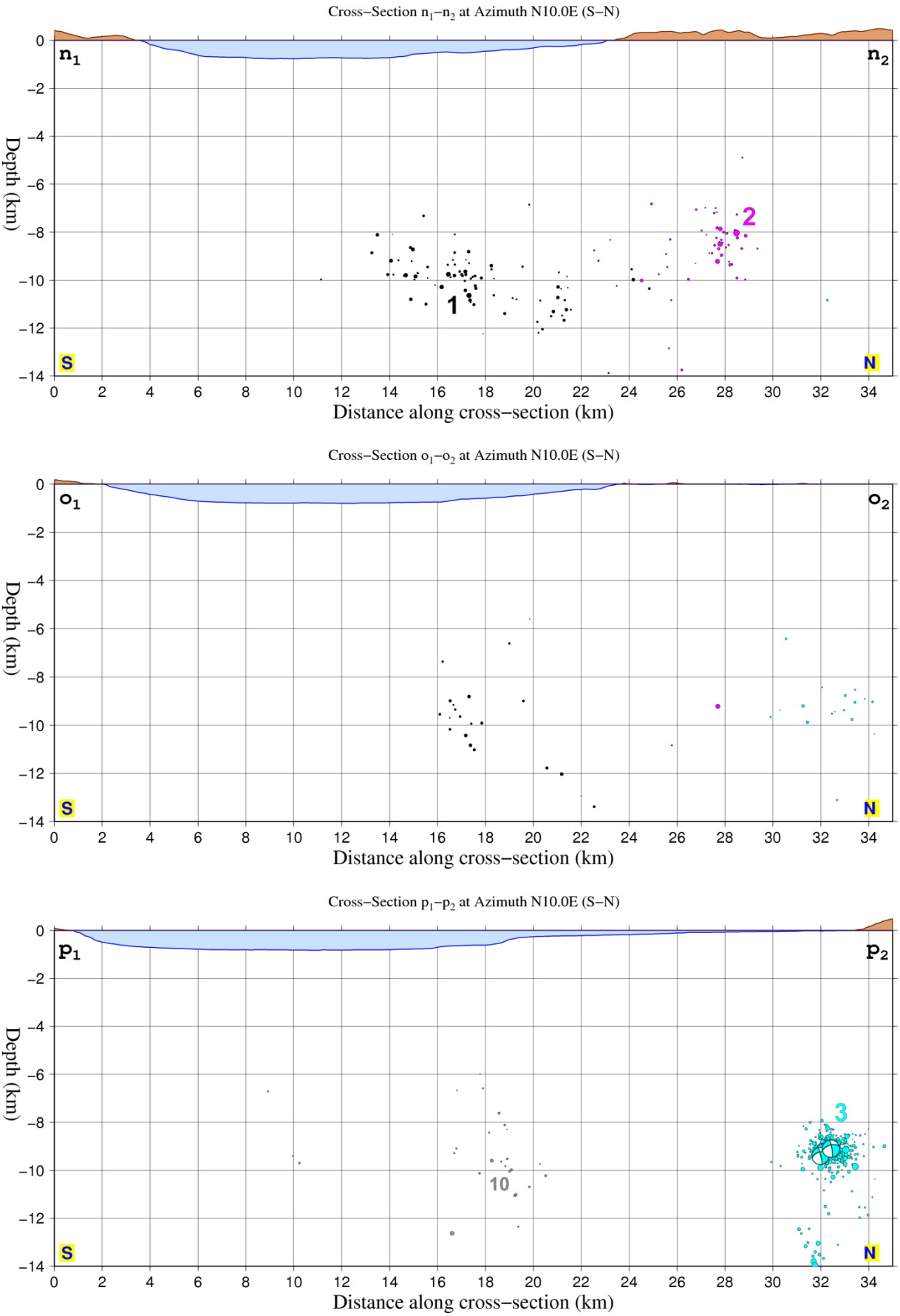


**Figure S13:** (continued)

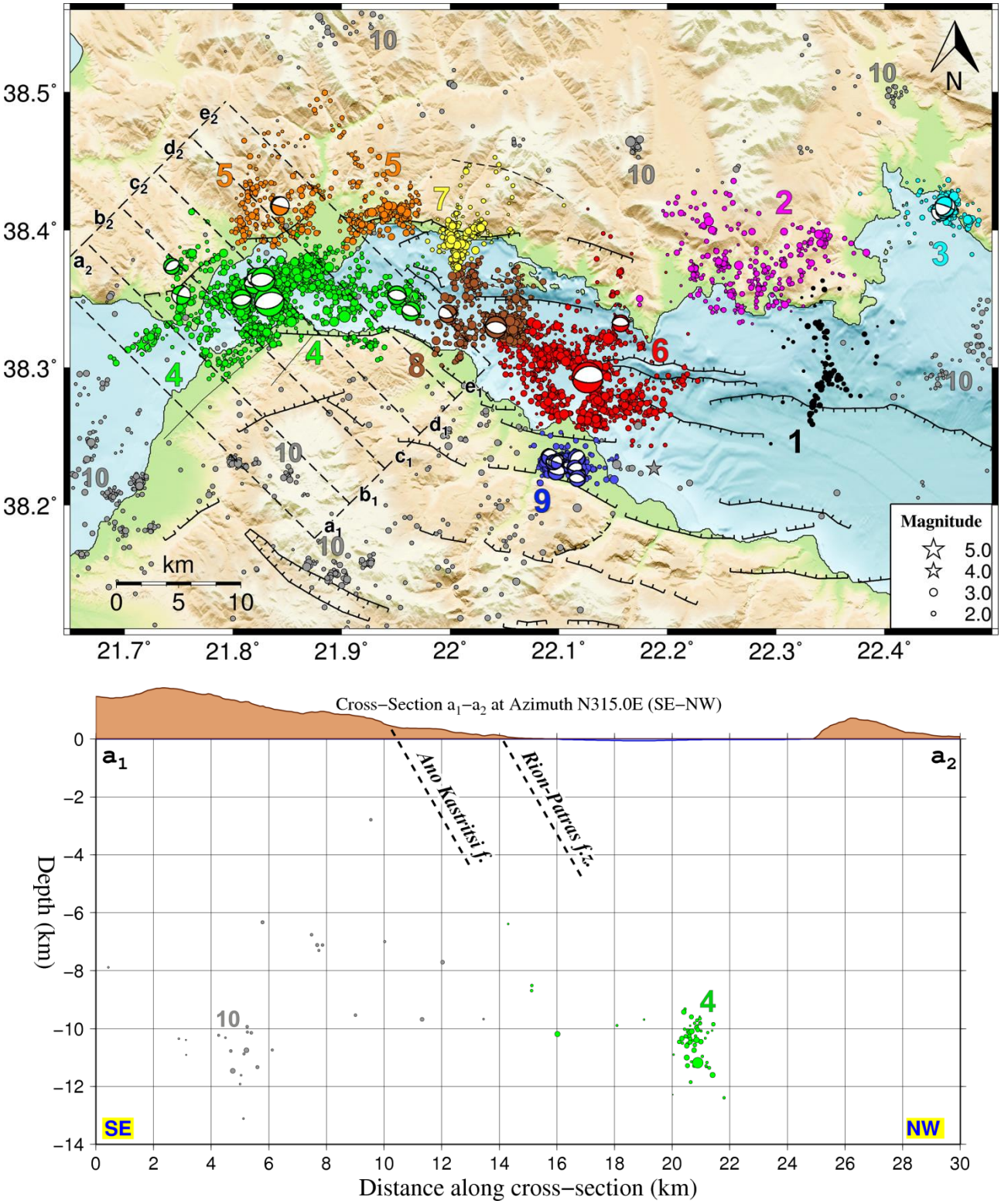


**Figure S14**. (Top) Map of relocated seismicity for 2013-2014 in the WGoC. Colours correspond to the 9 spatial groups in which the dataset was divided, along with the "miscellaneous" group #10 (gray). Beachballs depict the focal mechanisms of major events (Table 1). (Bottom panels) vertical cross-sections $a_1$-$a_2$ to $e_1$-$e_2$, drawn in a N315°E direction, corresponding to the dashed rectangles shown on the map (top). Beachballs depict the far hemisphere projections of focal mechanisms for major events. Black dashed lines at the top of the cross-sections indicate the position of mapped active faults with inferred extension at a 60° dip. For mapped faults' names refer to Figure 1.

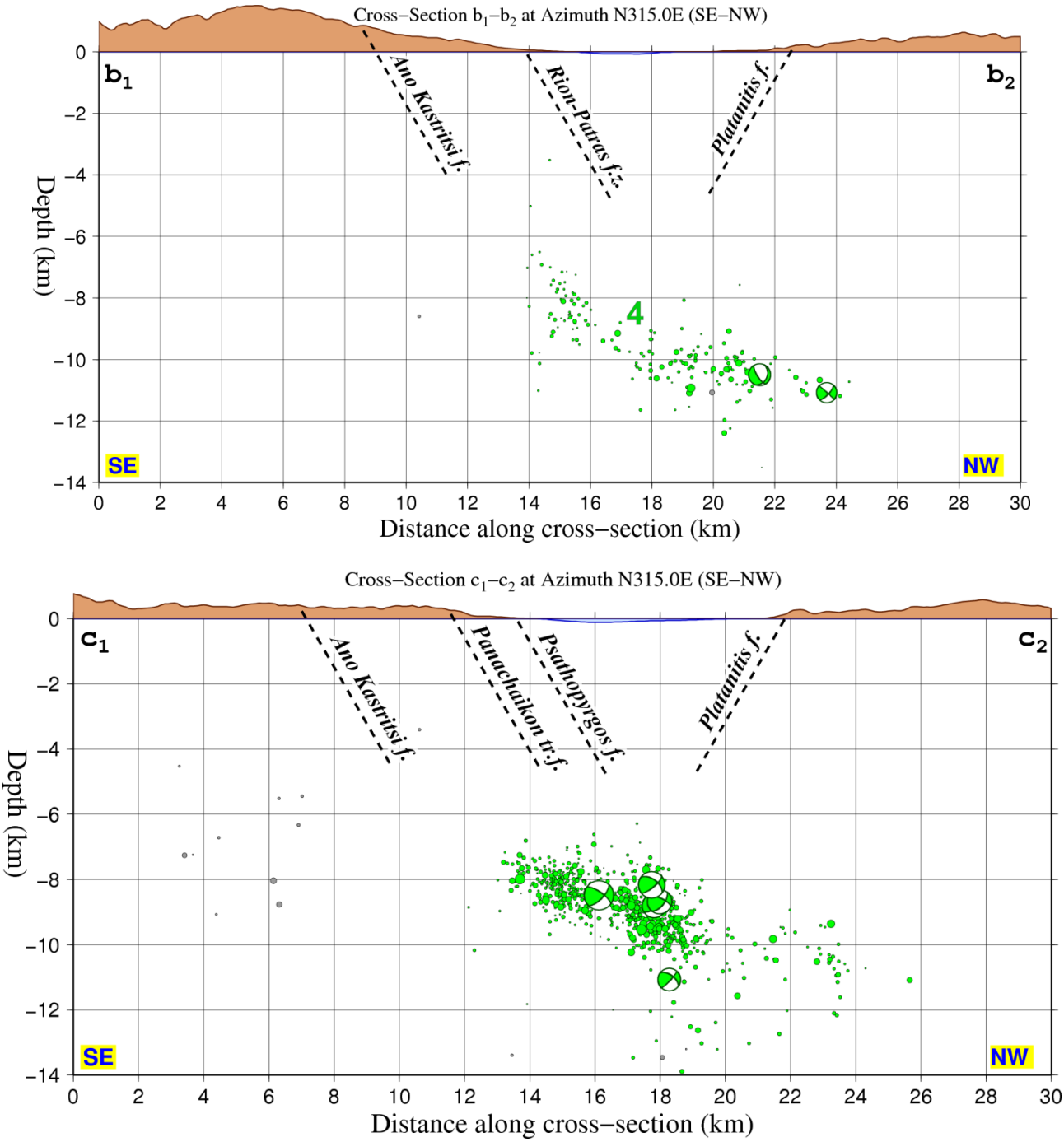


**Figure S14:** (continued)

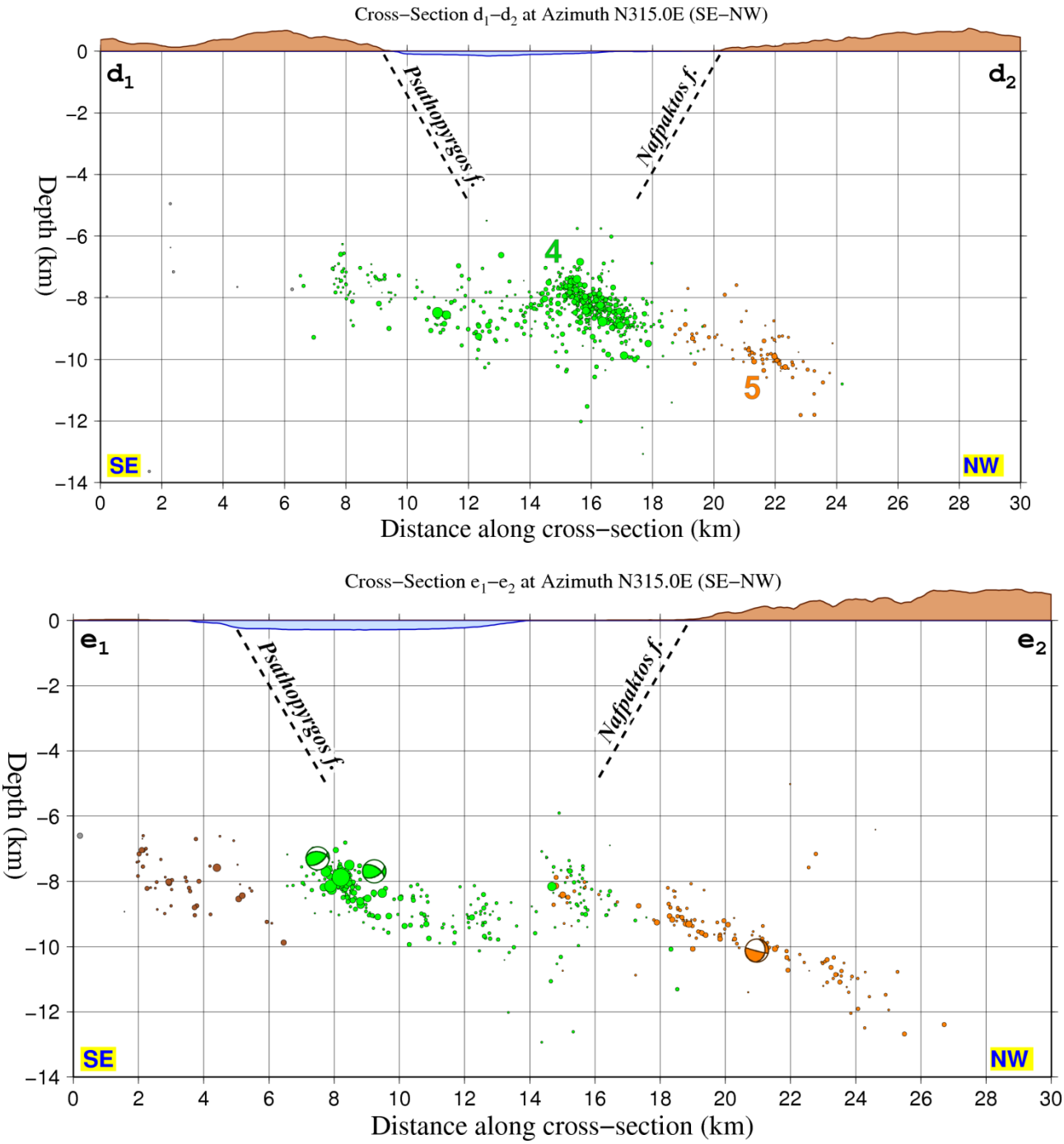


**Figure S14:** (continued)

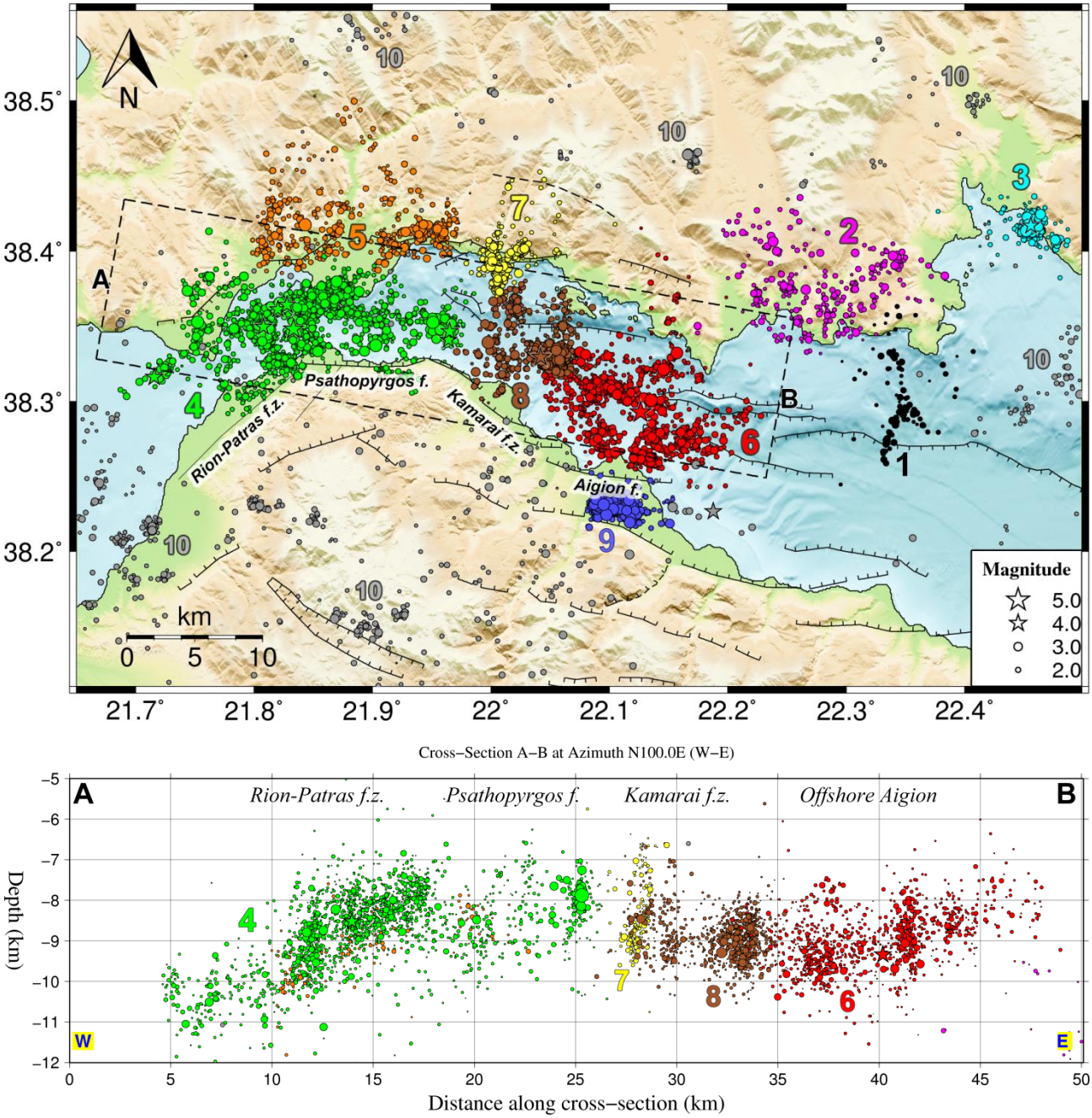


**Figure S15**. (Top) Map of relocated seismicity for 2013-2014 in the WGoC. Colours correspond to the 9 spatial groups in which the dataset was divided, along with the "miscellaneous" group #10 (gray). (Bottom panel) Vertical cross-section A-B, drawn in a N100°E direction, corresponding to the dashed rectangle shown on the map (top). The y-axis of the cross-section is exaggerated. The Kamarai fault zone (f.z.) comprises Lambiri, Selianitika and Fasouleika faults.

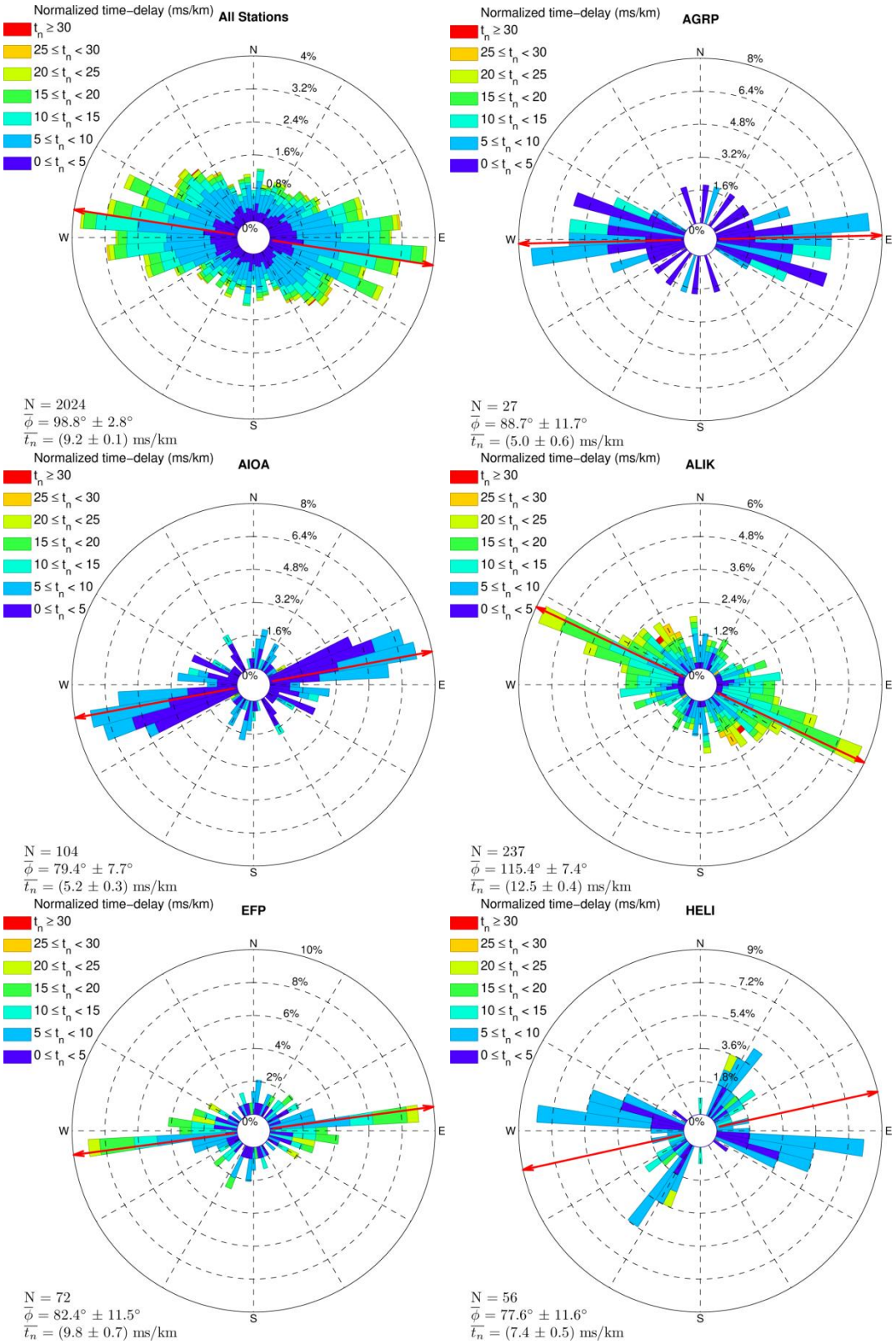


**Figure S16:** Rose diagrams of the distribution of the fast shear-wave polarization angle $\varphi$ for valid measurements with grade A (best) to C (acceptable) from Catalogue 1 (only manually located / relocated events) per station (station code shown on top of each diagram). Colours correspond to the respective normalized time-delay $t_n$. The red arrows indicate the average $\varphi$ direction.

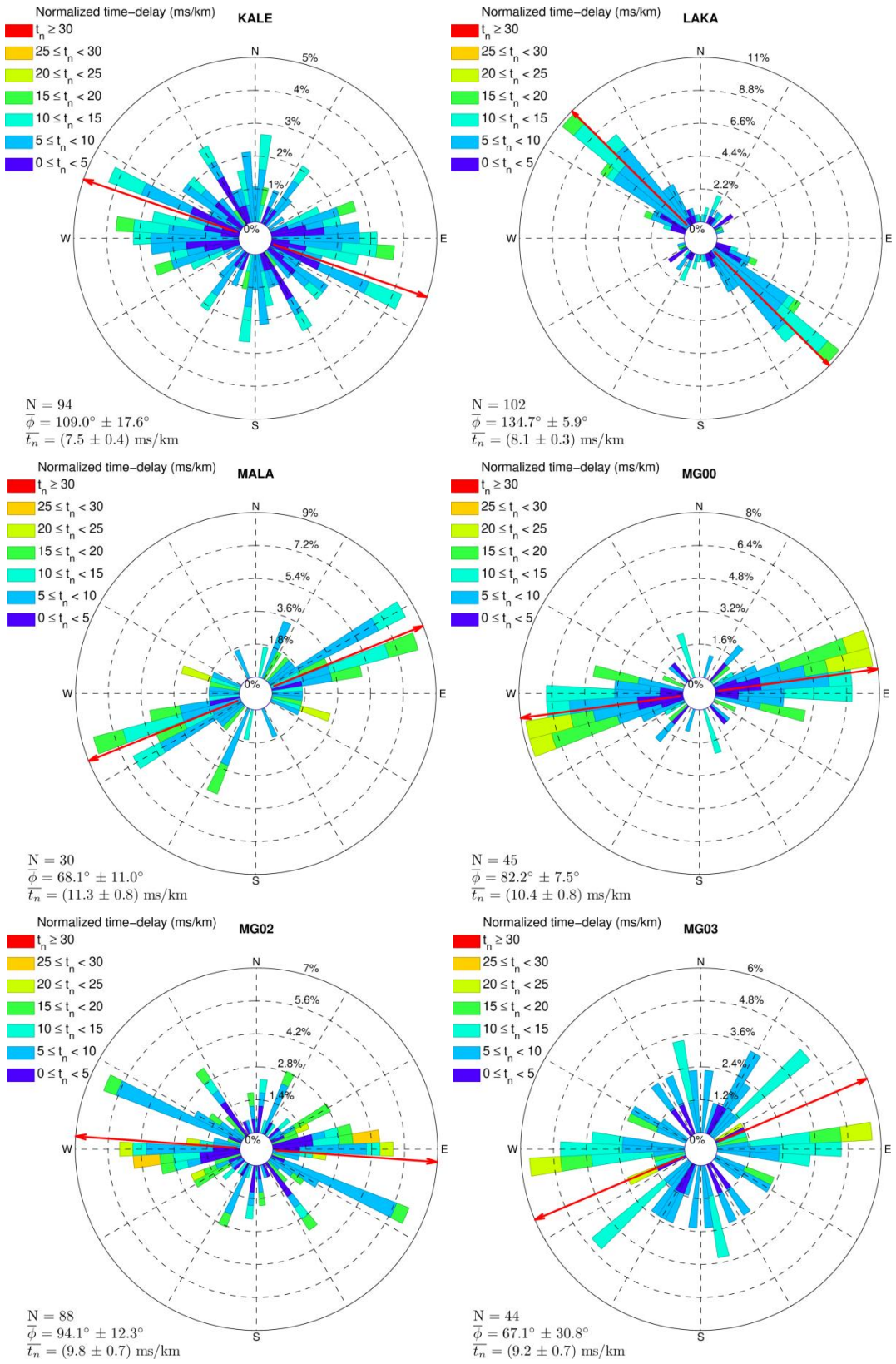


**Figure S16:** (continued)

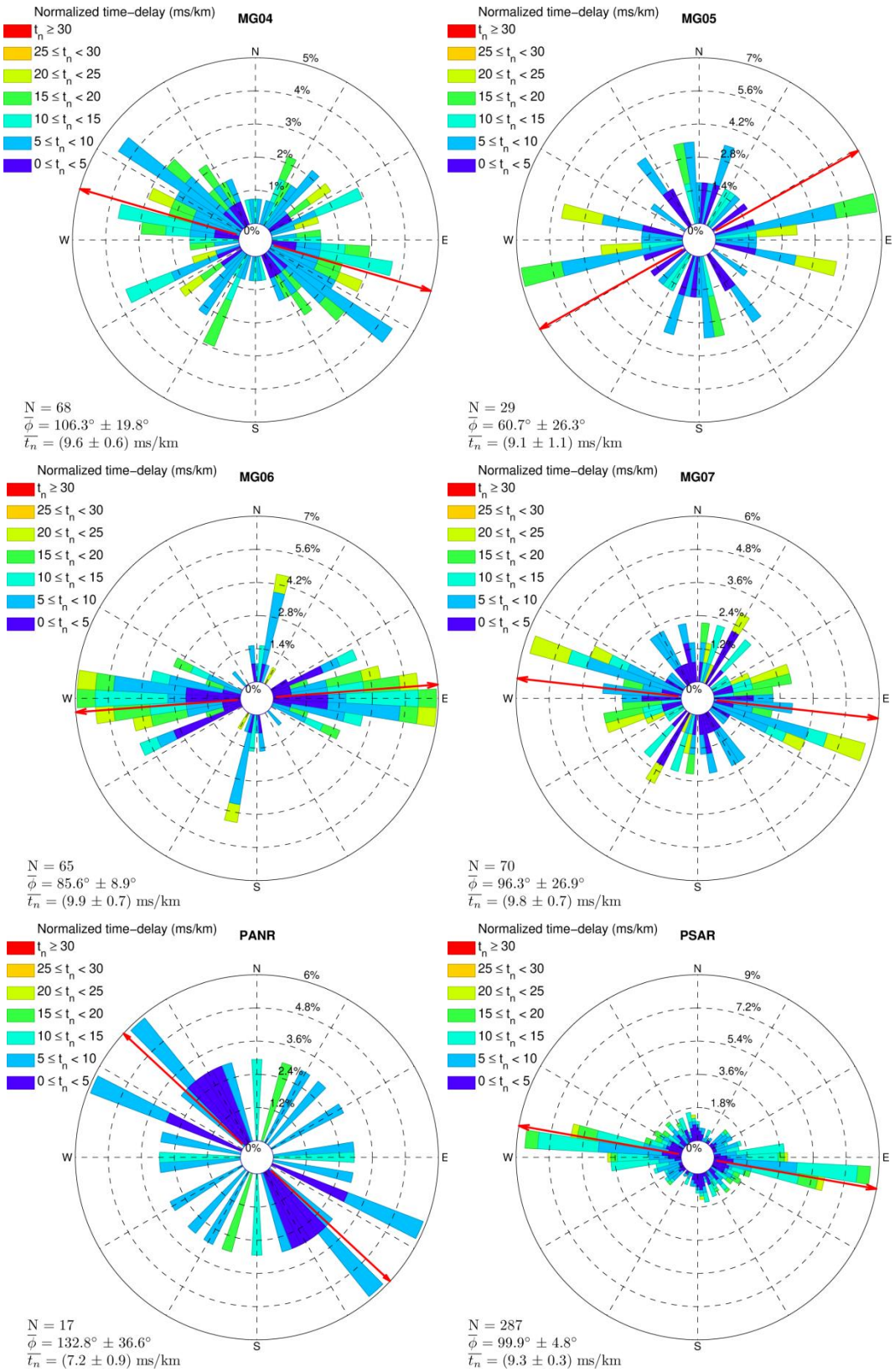


**Figure S16:** (continued)

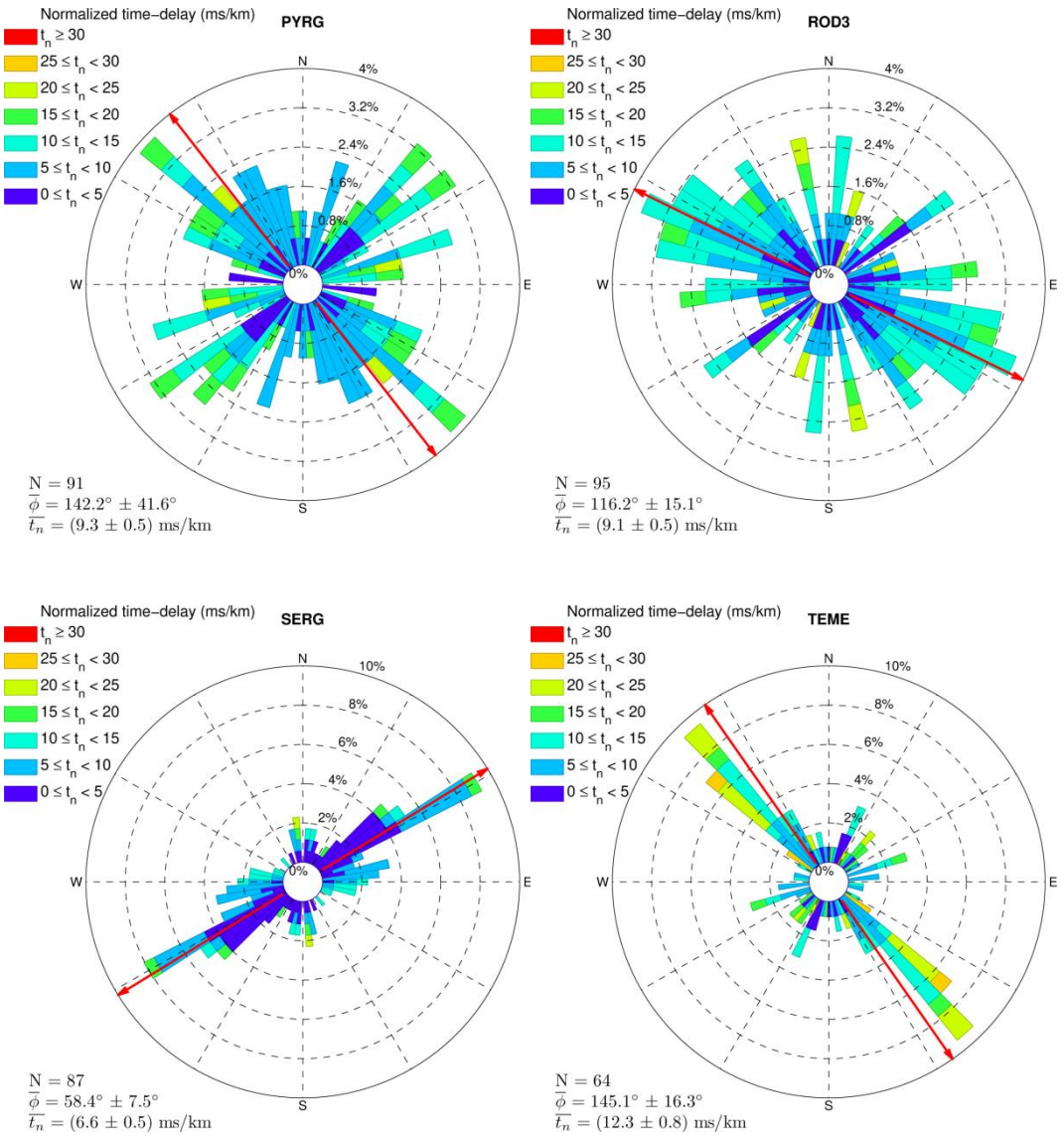


**Figure S16:** (continued)

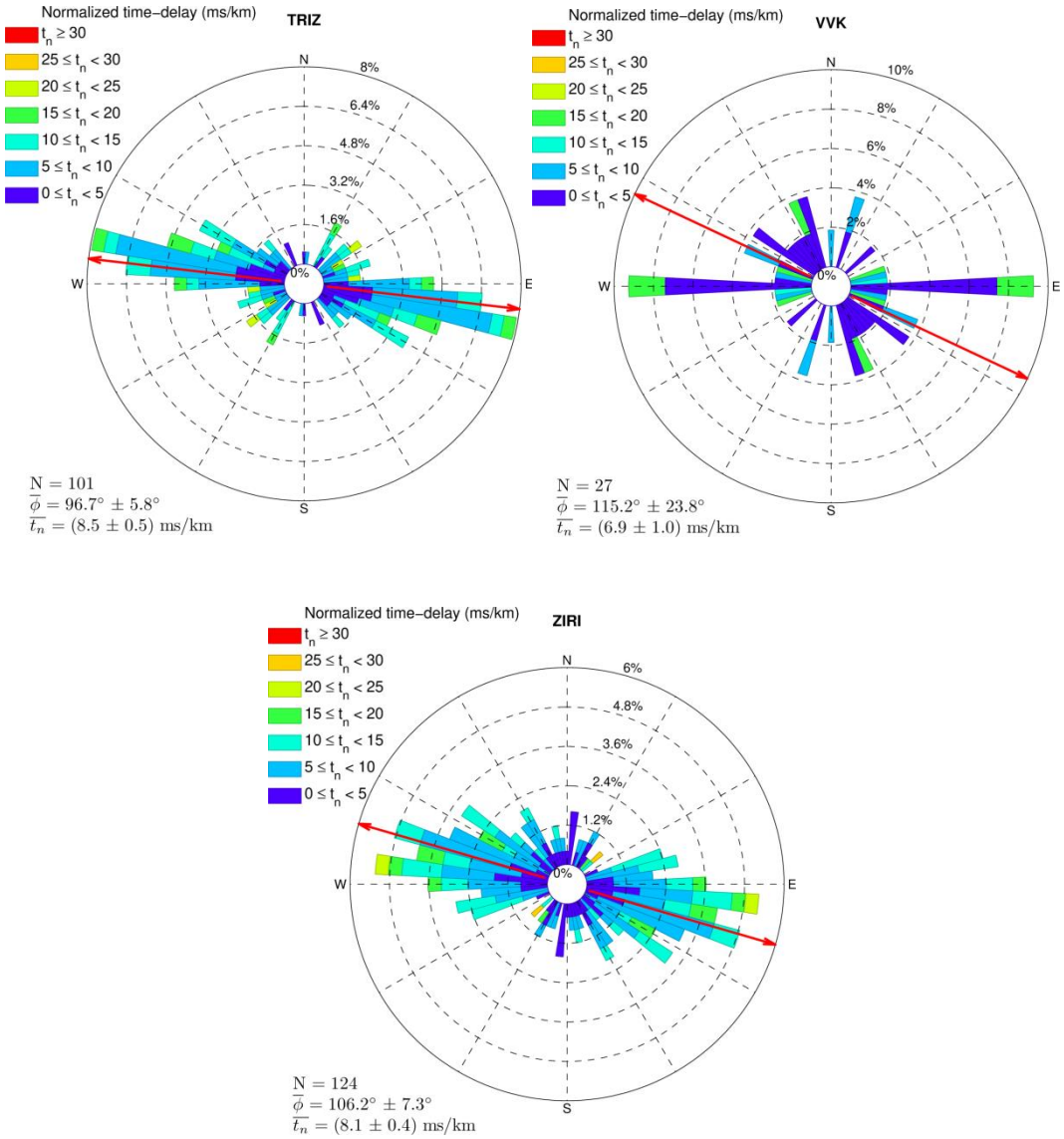


**Figure S16:** (continued)

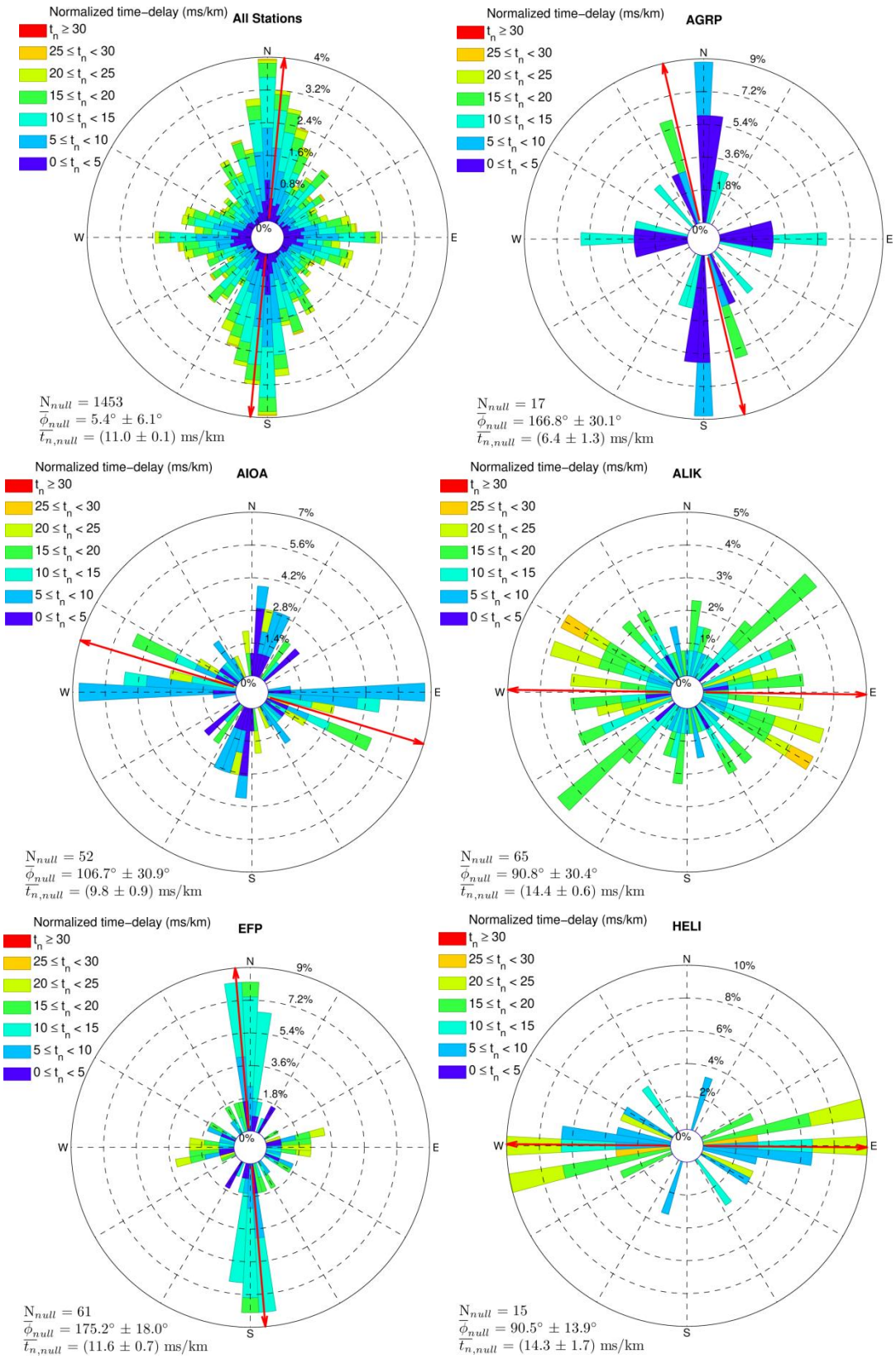


**Figure S17:** Rose diagrams of the distribution of the polarization angle $\varphi$ for null measurements (where $\varphi$ is in the range of $p \pm 10°$ or $(p+90°) \pm 10°$) from Catalogue 1 (only manually located / relocated events) per station (station code shown on top of each diagram). Colours correspond to the respective normalized time-delay $t_n$. The red arrows indicate the average $\varphi$ direction of null measurements.

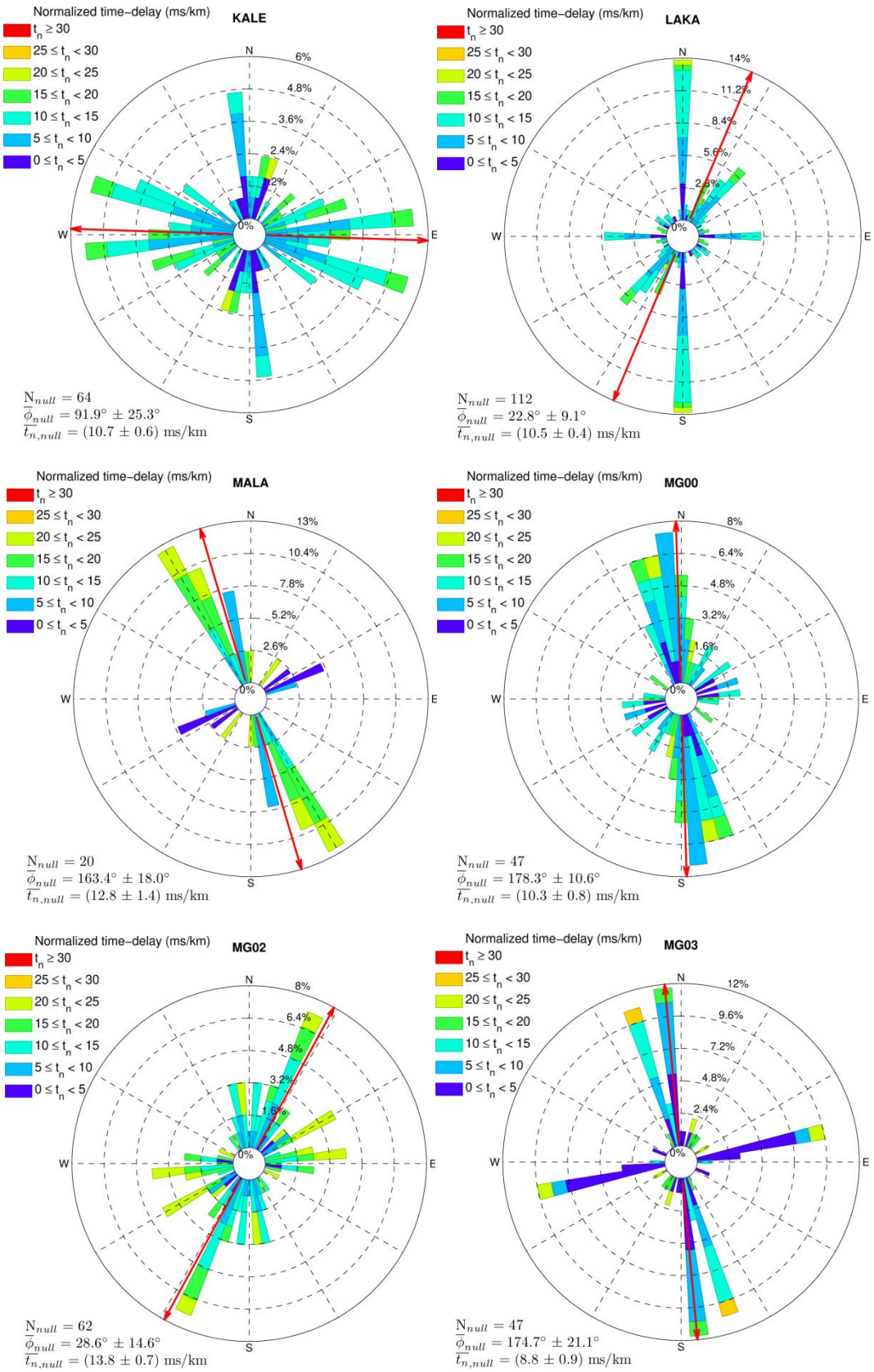


**Figure S17:** (continued)

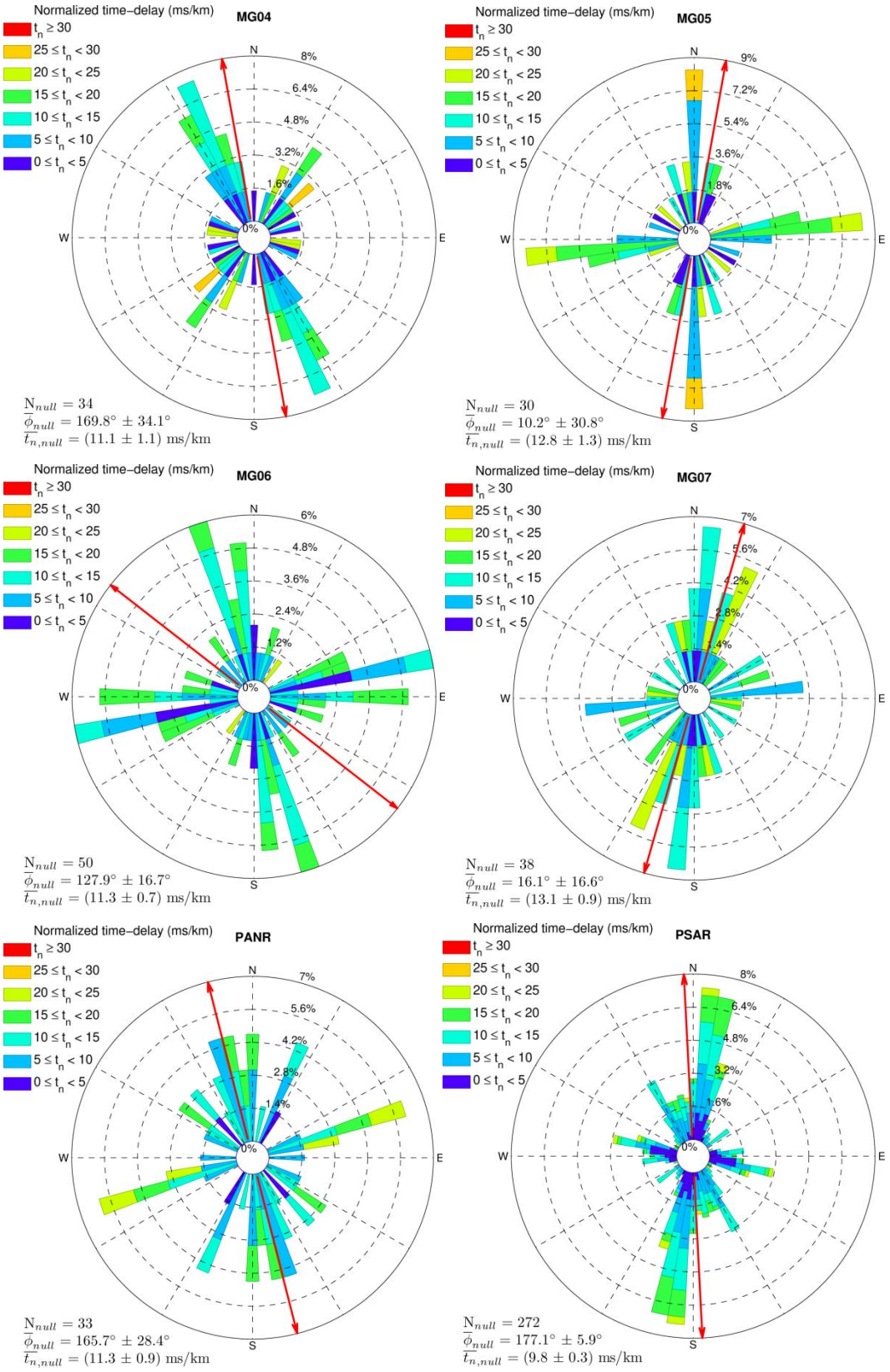


**Figure S17:** (continued)

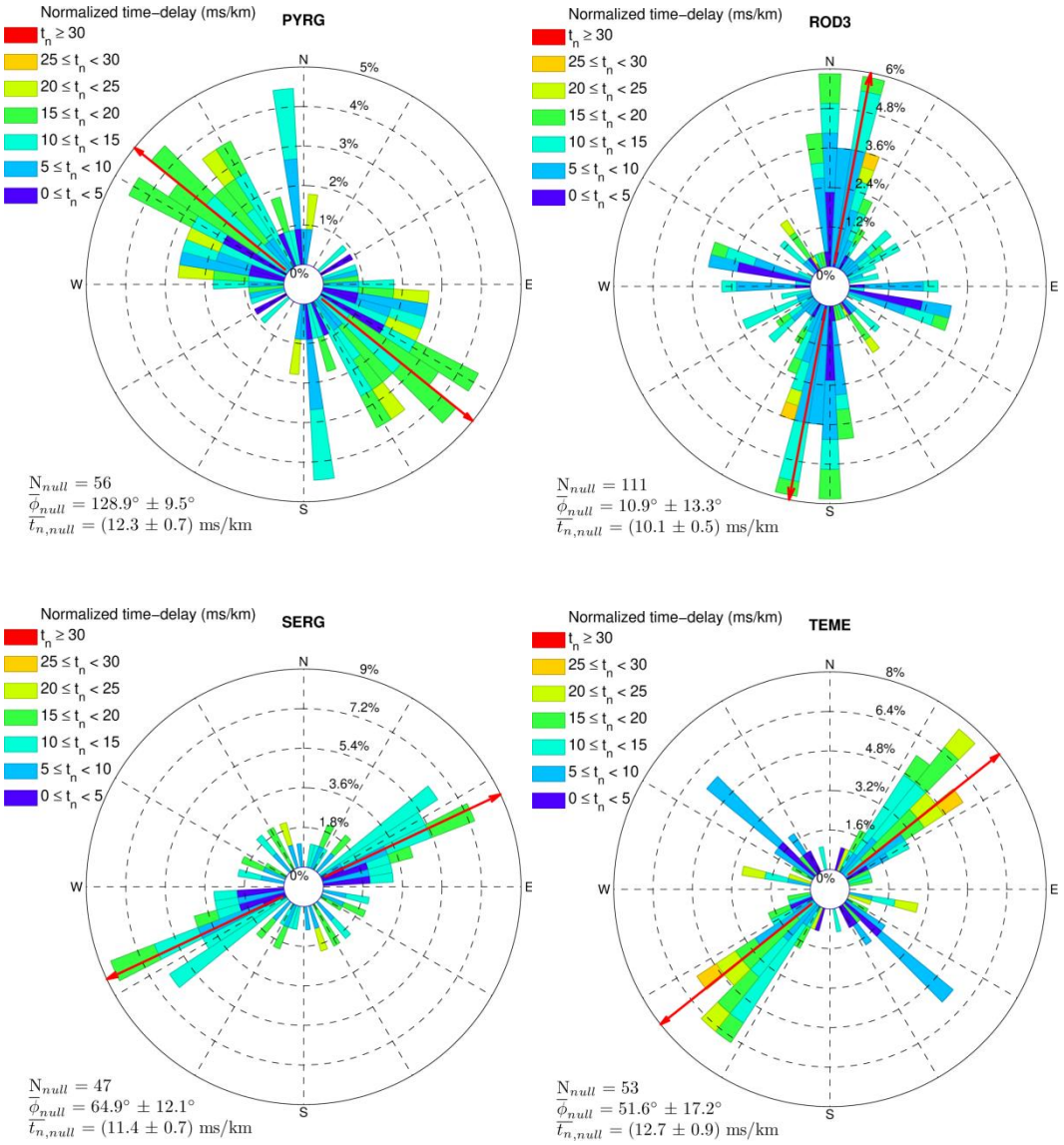


**Figure S17:** (continued)

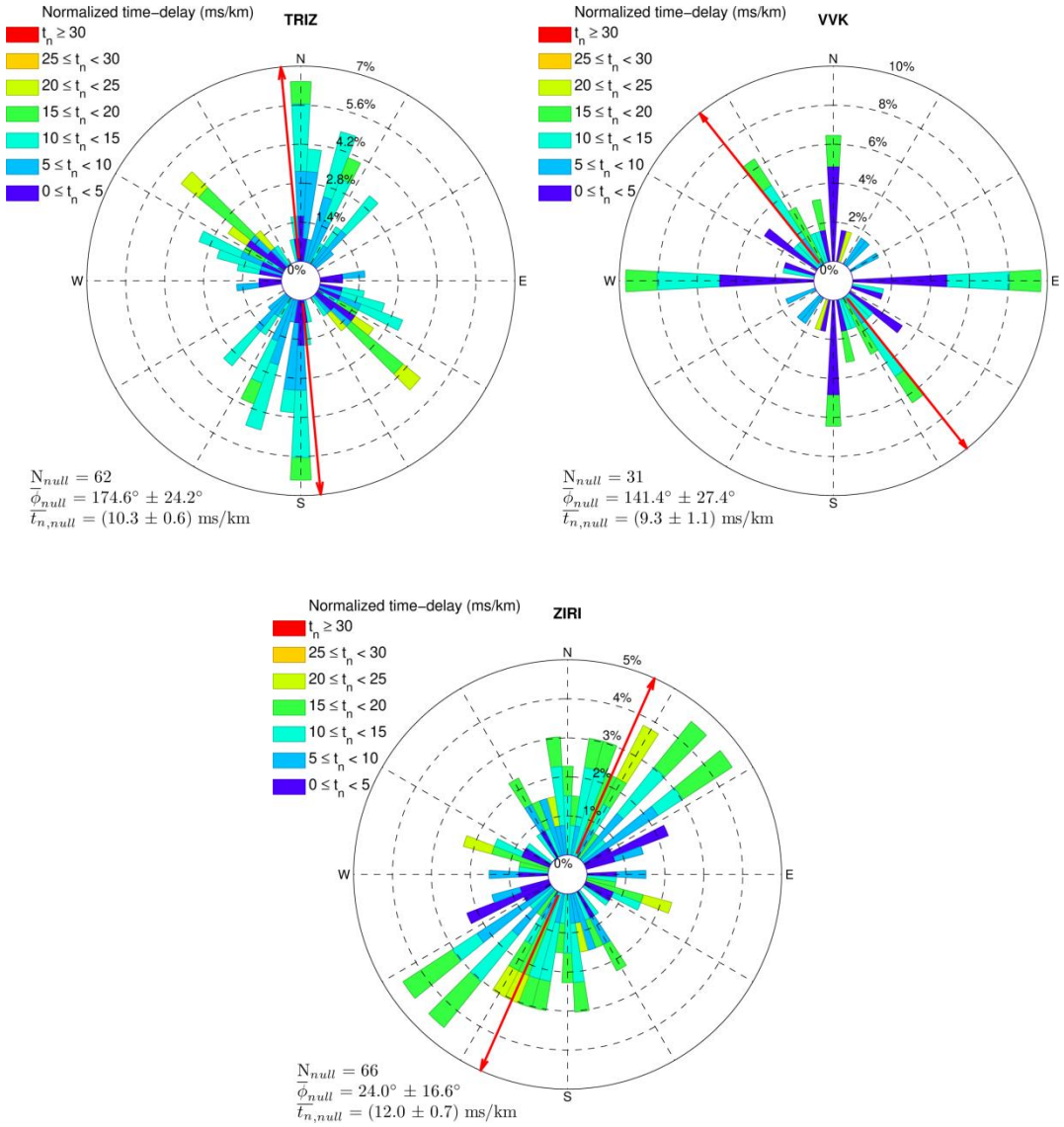


**Figure S17:** (continued)

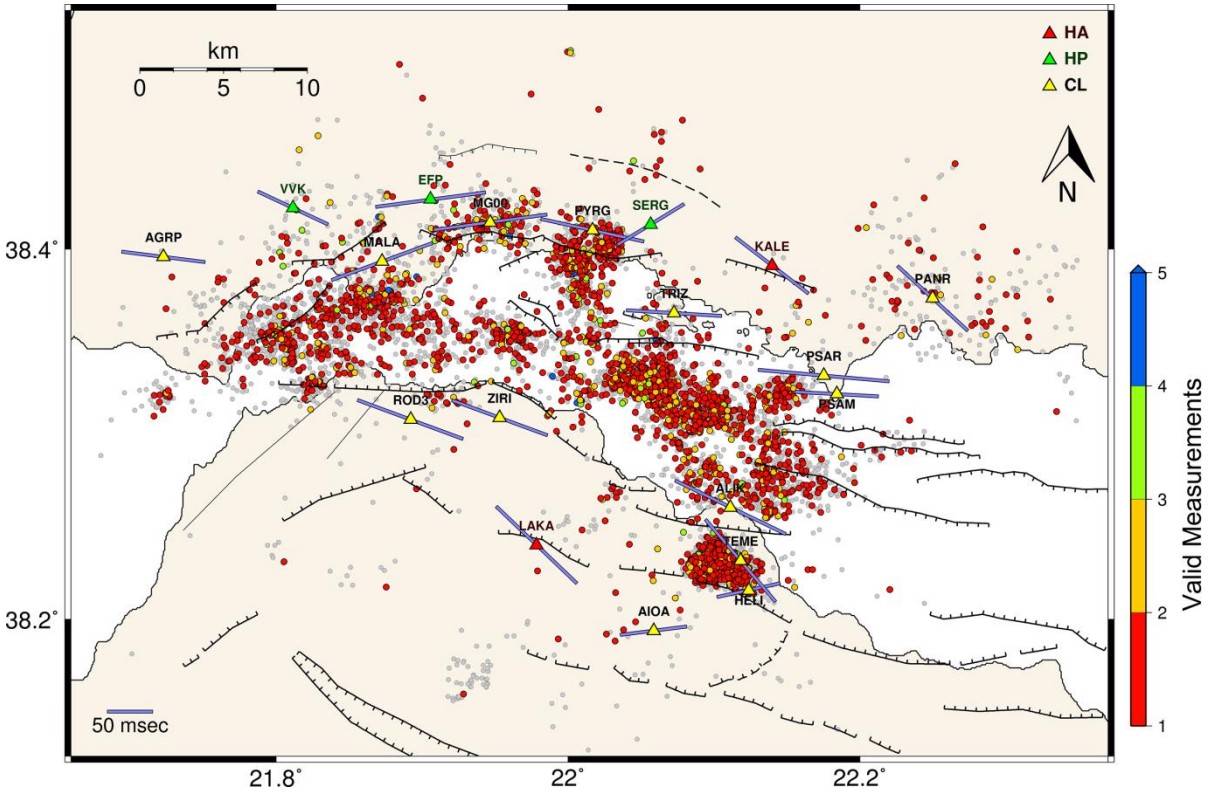


**Figure S18.** Map of candidate events for SWS measurements from Cat3 (manual and automatic) in the WGoC during 2013-2014. Blue lines represent the average fast S-wave polarization direction, $\varphi$ (orientation), and time-delay, $t_d$ (length), at the respective station (triangle, coloured according to network code). Coloured circles correspond to events with valid SWS measurements (grade A to C), whereas gray circles are events without valid measurements (only D, E or null).

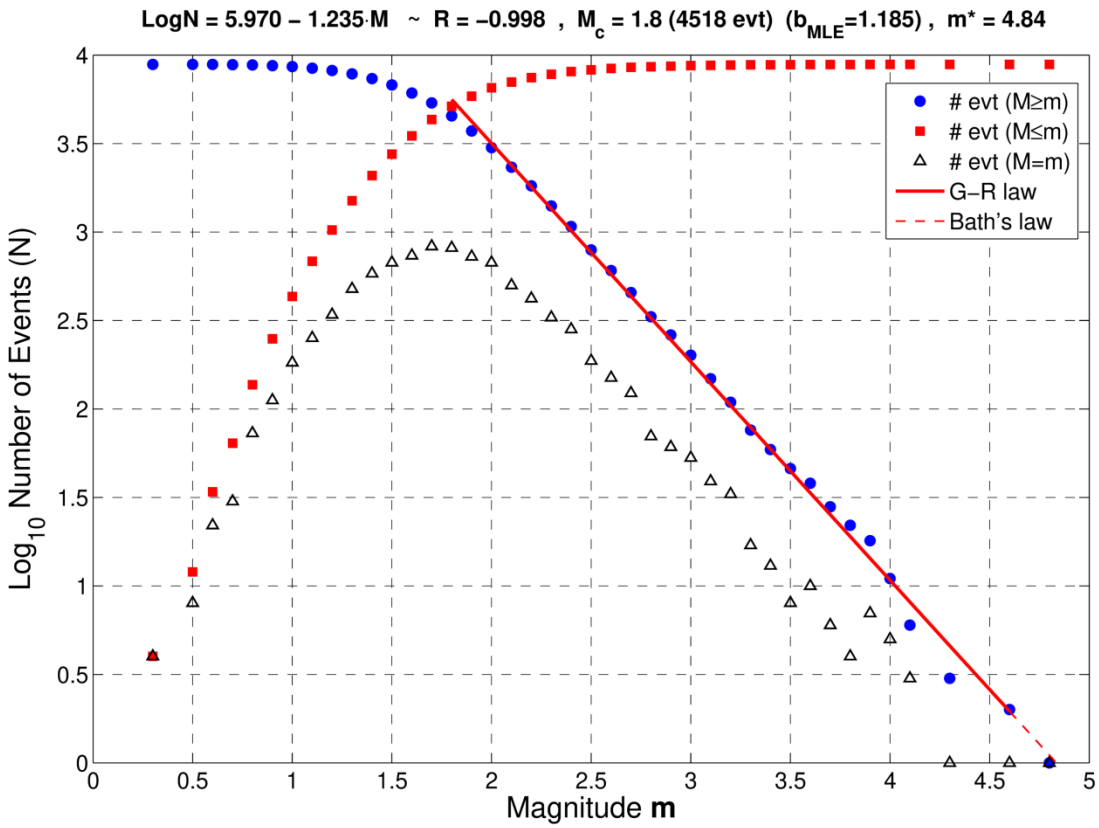


**Figure S19.** Gutenberg-Richter law for the seismicity of Catalogue 1. $M_c$=1.8 is the magnitude of completeness. The b-value is calculated as 1.235±0.015 from linear regression (correlation coefficient $R$=-0.998) or $b_{MLE}$=1.185 from the maximum likelihood method.

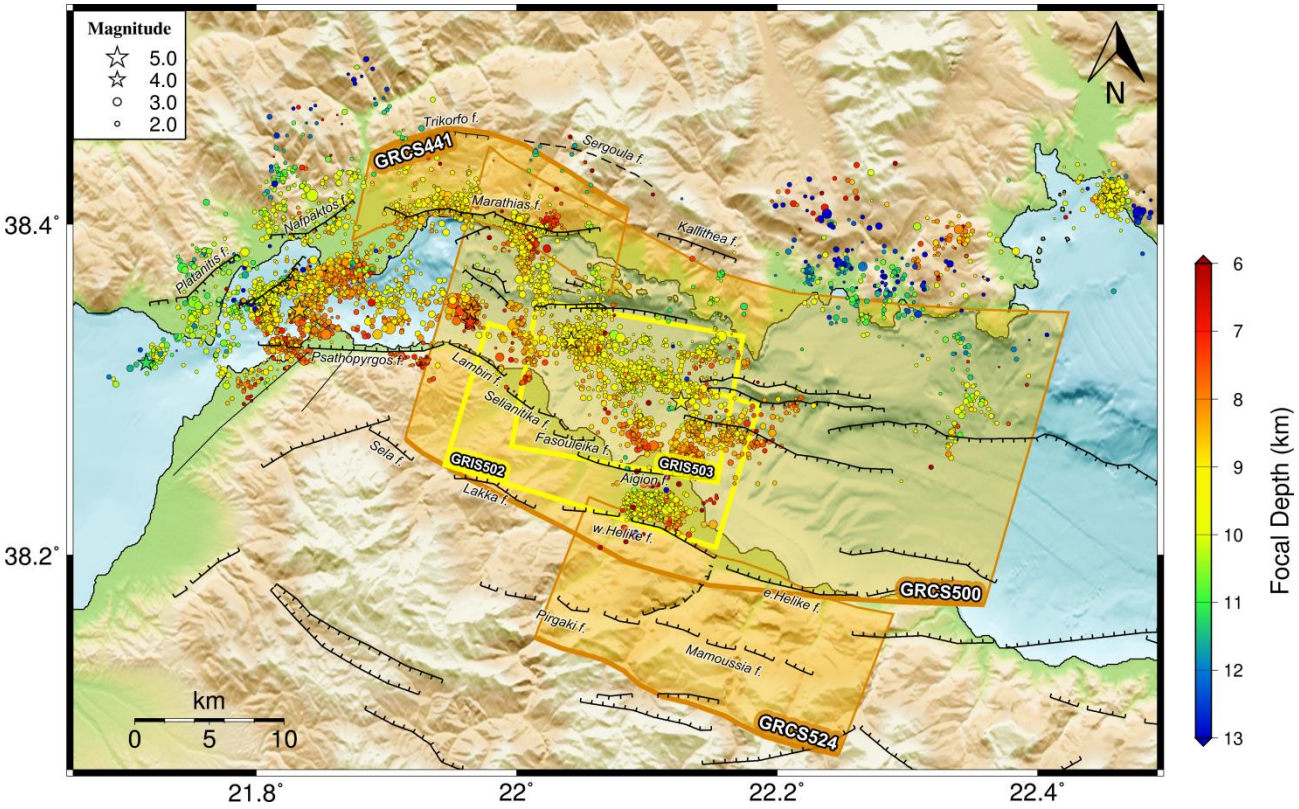


**Figure S20.** Composite Seismogenic Sources (orange) and Individual Seismogenic Sources (yellow) from the Greek Database of Seismogenic Sources (GreDaSS, Caputo & Pavlides, 2013) in the WGoC area, mentioned in the main text. GRCS441: Trikorfo source, associated with Trikorfo and Sergoula faults, GRCS500: South Corinth Gulf source, associated with Sela, Lakka, w.Helike and e. Helike faults, GRCS524: Mamoussia source, associated with Pirgaki and Mamoussia faults, GRIS502: west Helike fault source, also associated with Lakka fault, GRIS503: Aigion fault source, also associated with Fasouleika and Selianitika faults.

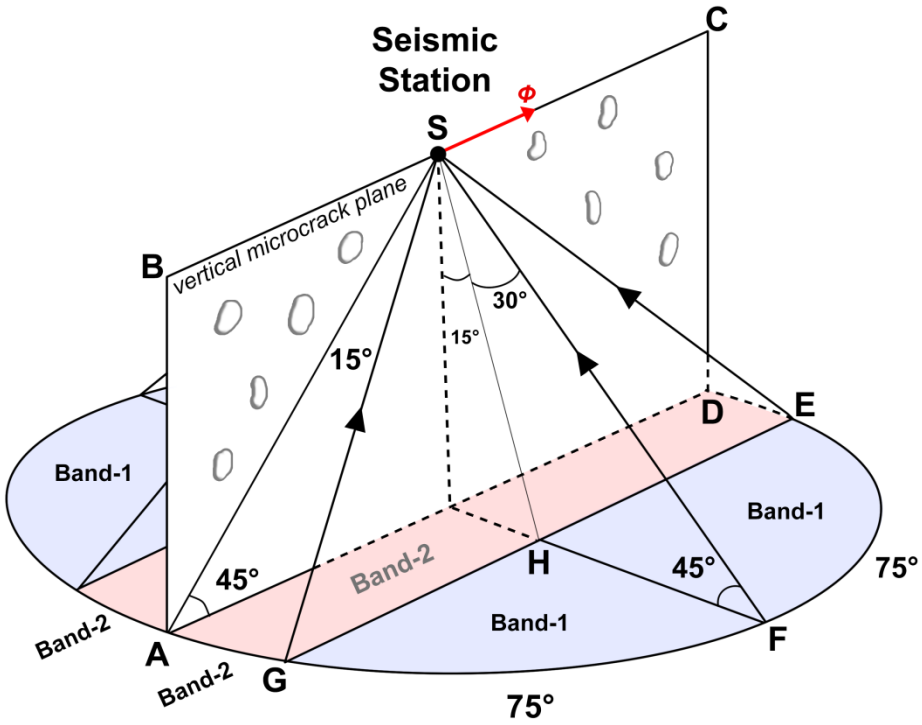


**Figure S21.** Schematic representation of Band-1 and Band-2 zones, modified after Crampin et al. (2013). The receiver at the surface is marked with S. The ABCD plane of vertically aligned microcracks is oriented towards the mean fast shear-wave polarization direction, $\Phi$. Band-1 contains seismic rays traveling towards the seismic station at directions contained within the solid angle EFGH-to-S (blue),at angles between 15° and 45° (shear-wave window) on either side of the crack-plane. Band-2 contains seismic rays that travel within the solid angle ADEHG-to-S (red) towards the seismic station, i.e. within ±15° from the crack-plane.

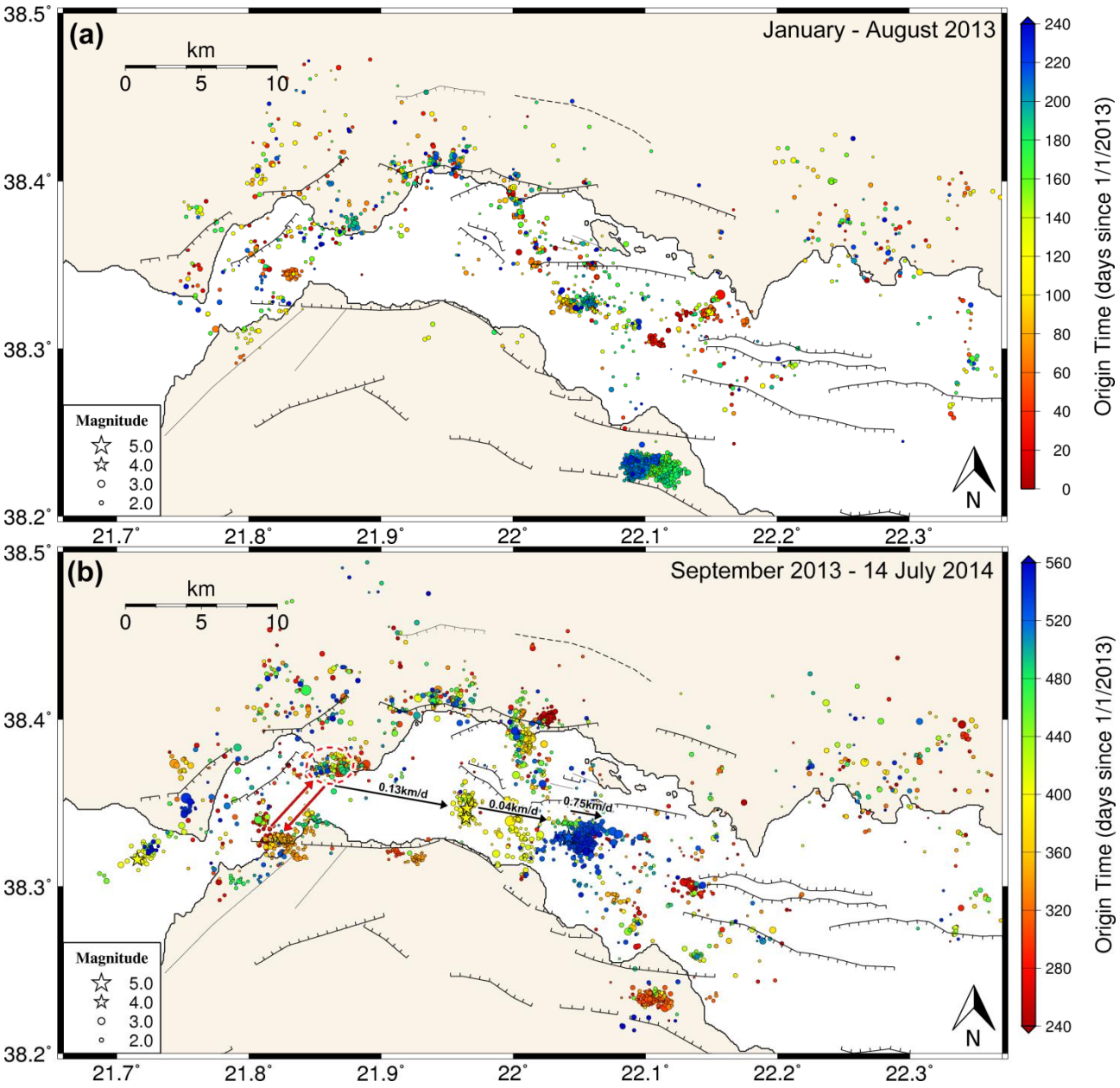


**Figure S22.** Maps of the temporal evolution of the 2013-2014 sequence in the WGoC (Catalogue 1, all spatial groups except #3 and #10). The colours represent relative origin time (see labels on the colour-scale of each panel). (a) January – August 2013: the map shows sporadic activity inside the gulf, with the most significant cluster being the 2013 Helike sequence. (b) September 2013 – 14 July 2014: several clusters were observed at the western part of group #4, with activity going back and forth as shown with the red arrows. The dashed red ellipse shows a possible source of fluid injection. The black arrows show the direction (N100°E) and speed of seismicity migration or inferred fluid diffusion (see Figure 5). Seismicity gradually migrated eastwards at ~0.13km/day, activating the clusters with yellow colour (days 380-400). Fluid diffusion at a rate of 0.04km/day towards N100°E precedes the triggering of the June 2014 sequence (dark blue), during which seismicity migration at 0.75 km/day was observed within the cluster (see also Figure A2).

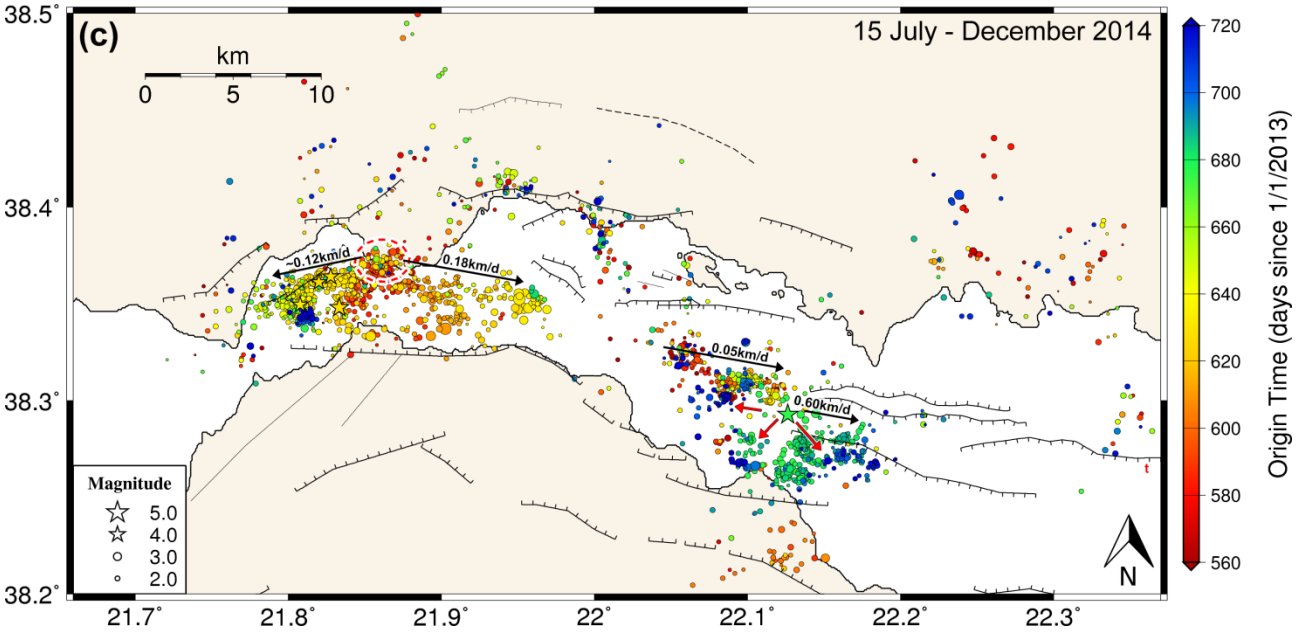


**Figure S22.** (continued). (c) 15 July – December 2014: bilateral seismicity migration observed in the spatial group #4, starting from the region marked with the red dashed ellipse (same as in panel b). Seismicity migration at a speed of 0.05km/day towards N100°E between groups #8 and #6 is marked with a black arrow. The 7 November 2014 $M_w$=4.8 event (green star) triggers seismicity mostly southwards.

## File M1: 3D Interactive Matlab Figure

File "M1_WGoC_3D_interactive.fig"

Interactive 3D visualization of the seismicity in the WGoC during 2013-2014 (Catalogue 1; see also Figure A5). The "3D View" menu at the top can be used to select different preset viewing angles, change the vertical exaggeration (the default one is x2) and the opacity of the digital elevation model (DEM). The "Layers" menu can be used to show or hide different layers, including the DEM, the coastline, the fault traces, the fault planes, the hypocenters and the planes associated with the observed seismicity. The user also has the option to modify the dip of the surface faults (default value is 60°) and the down-dip depth (the default value is 4km). The hypocenters and their associated structure planes can be shown or hidden either globally or per spatial group ("Datasets" sub-menu). Hypocenter colours are as defined in Figure 2 per spatial group. Earthquakes with $M_w \geq 4.0$ are marked with stars.

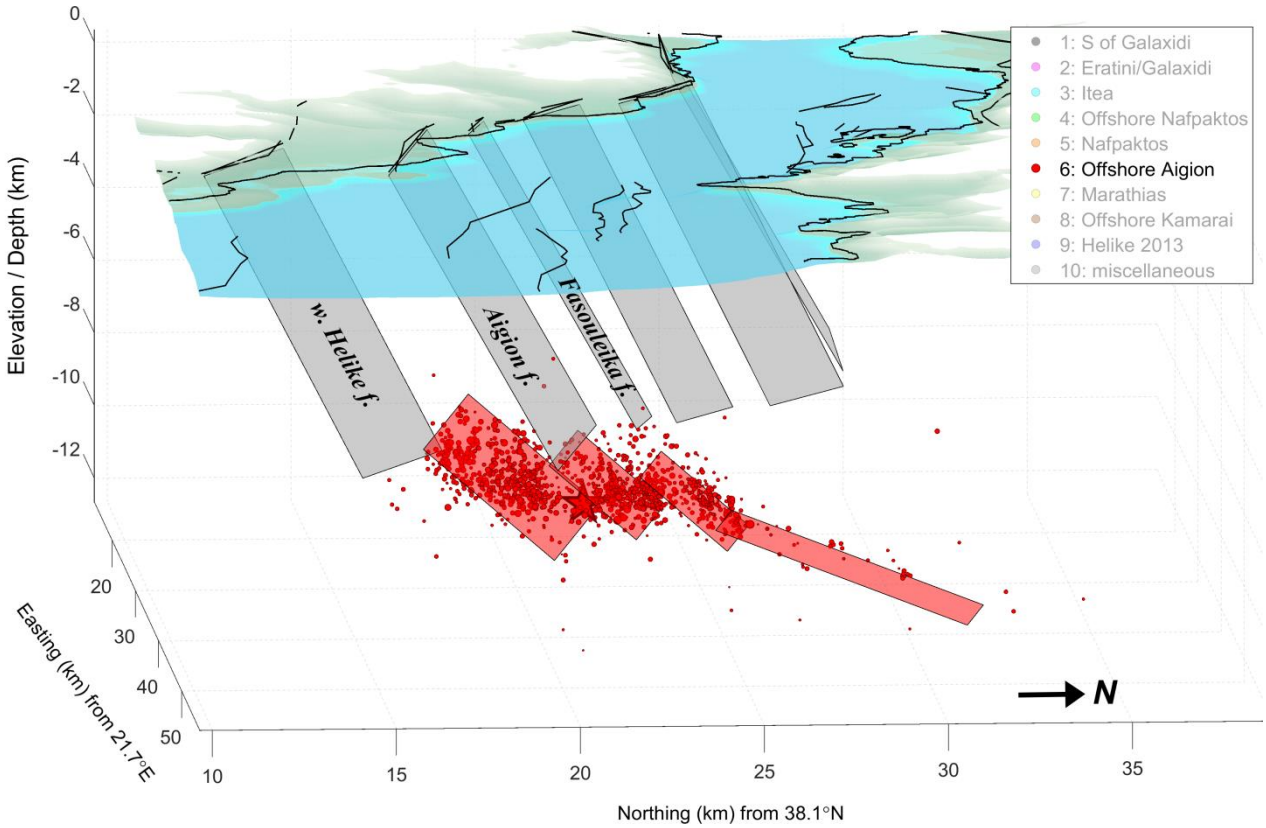


**Figure S23.** Annotated snapshot of the interactive 3D figure (File M1), showing the spatial group #6 and associated structure planes, along with selected surface fault planes (gray) extended downwards to the depth of 8 km at a 60° dip. The view is towards west. No vertical exaggeration has been applied.

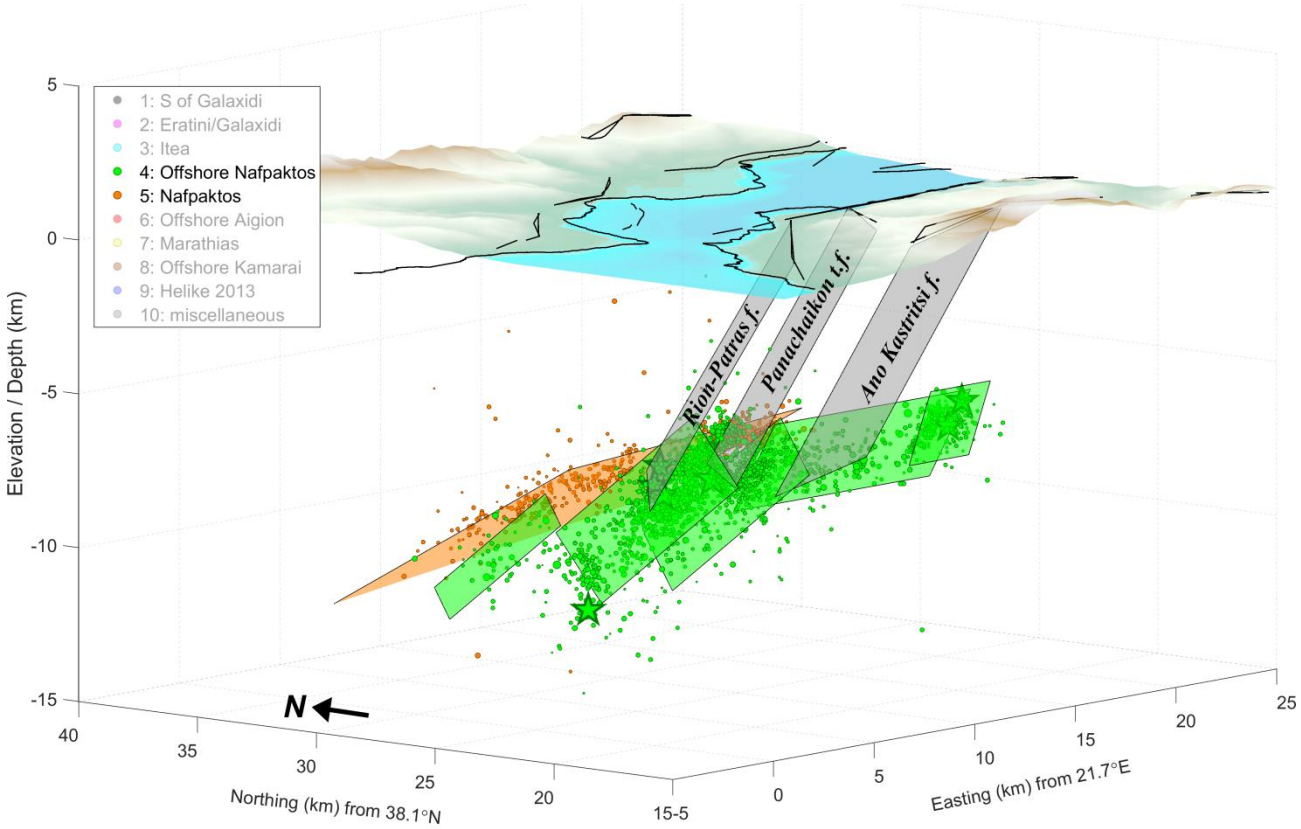


**Figure S24.** Annotated snapshot of the interactive 3D figure (File M1), showing the spatial groups #4 (green) and #5 (orange) and proposed associated structure planes. Selected surface fault planes (gray) are extended downwards to the depth of 8 km at a 60° dip. The view is towards north-east. No vertical exaggeration has been applied.

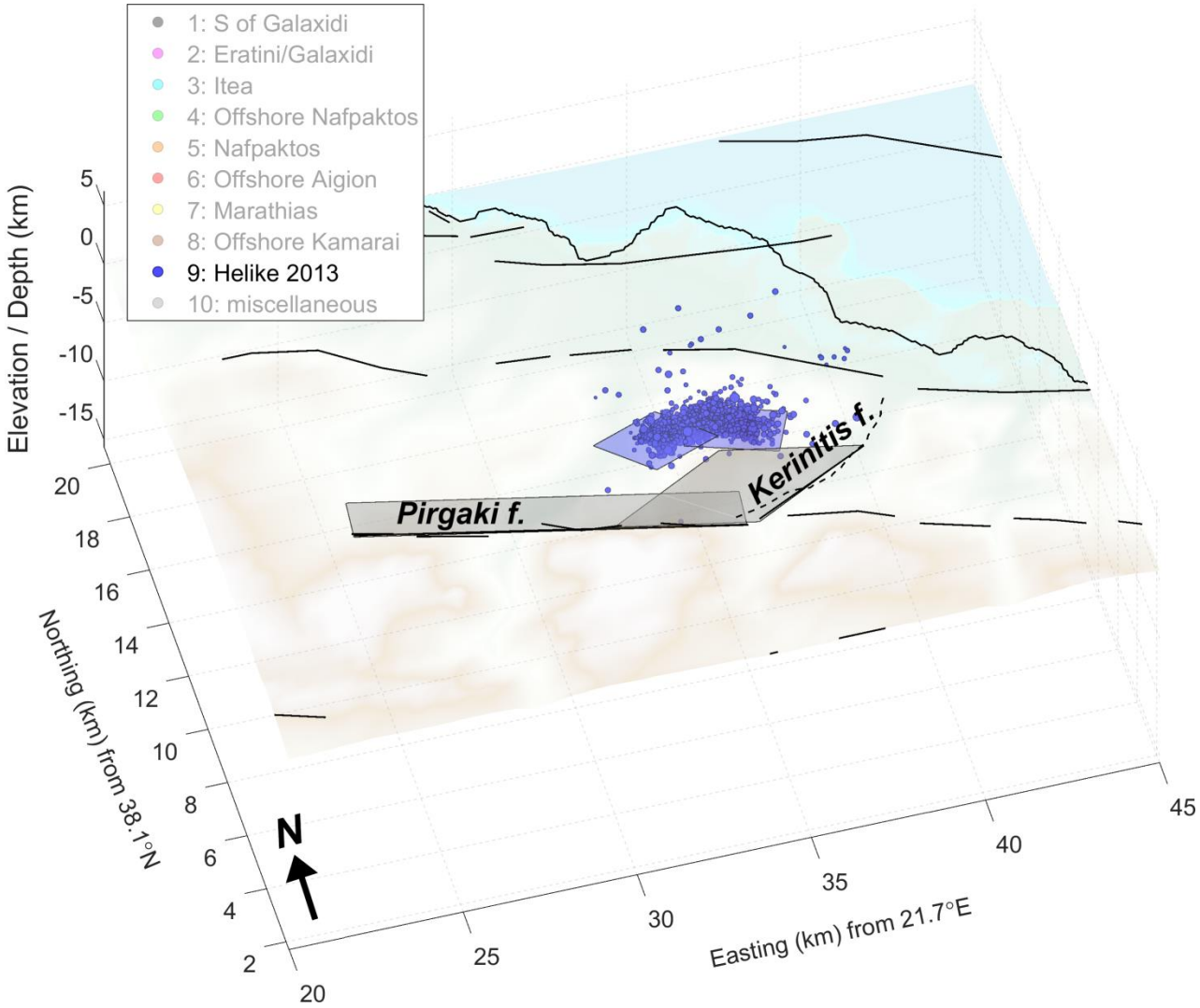


**Figure S25.** Annotated snapshot of the interactive 3D figure (File M1), showing the 2013 Helike swarm (spatial group #9) and associated structure planes that were activated (blue). The surface fault planes (gray) of Pirgaki and Kerinitis faults are shown in gray. The view is downwards and towards NNE. Although the swarm is mainly associated with the north-dipping Pirgaki fault, it also contained events with oblique-normal focal mechanisms, likely related to NW-dipping structures sub-parallel to Kerinitis fault (Kapetanidis et al., 2015).

## Dataset D1: Catalogue of seismicity

Excel file "D1_wgoc2013-2014_seismicity_catalogue.xlsx".

Seismicity catalogue of the Western Gulf of Corinth for the period of 2013-2014.

Sheet 1: "Catalogue 1" of manually analyzed events.

Sheet 2: "Catalogue 2" of automatically analyzed events.

Column description:

1) event-code: characteristic unique code label for each event in a yyyy-mm-dd-HH-MM-SS format, also used in Dataset D2.
2-7) Year, Month, Day, Hour, Minute, Second of origin time.
8) Latitude (°N).
9) Longitude (°E).
10) Focal Depth (km).
11) Moment Magnitude ($M_w$) calculated using spectral fitting, where available.
12) Cluster ID: spatial group number, where available (see Figures 2 and 4).
13) Type: "located", for locations provided by HypoInverse (Catalogue 1), "relocated" for relocated solutions with HypoDD (Catalogue 1) or "automatic" for solutions of Catalogue 3 with HypoInverse.

## Dataset D2: Anisotropy measurements

Excel file "D2_wgoc2013-2014_sws_data.xlsx".

Dataset of shear-wave splitting measurements (Catalogue 3).

Each excel sheet corresponds to a specific station. Measurements with grade A to D are included.

Column description:

1) Station: station-code.
2) event-code: characteristic unique code label for each event in a yyyy-mm-dd-HH-MM-SS format, also used in Dataset D1.
3) Catalogue #: Catalogue number 1 (manual) or 2 (automatic).
4) CLID: Cluster ID, spatial group number, where available (see Figures 2 and 4).
5-10) Year, Month, Day, Hour, Minute, Second of origin time.
11) Latitude (°N).
12) Longitude (°E).
13) Focal Depth (km). For events of Catalogue 2, the focal depth replaced with the average focal depth of the events with neighboring epicenters of Cat1, as described in the main text.
14) Moment Magnitude ($M_w$) calculated using spectral fitting, where available.
15) baz (deg): backazimuth of event.
16) incidence (deg): angle of incidence at the surface.
17) Ep.Dist. (km): epicentral distance.
18) Hyp.Dist. (km): hypocentral distance.
19) Phi (deg): polarization direction $\varphi$ of fast shear-wave.
20) dPhi (deg): uncertainty of $\varphi$ (according to the 95% c.i. of $\lambda_2$).
21) Td (ms): time-lag, $t_d$, between fast and slow shear-waves.
22) dTd (ms): uncertainty of $t_d$ (according to the 95% c.i. of $\lambda_2$).
23) Tn (ms/km): normalized time-delay, $t_n$.
24) dTn (ms/km): uncertainty of the normalized time-delay.
25) p (deg): polarization direction of the source, after being corrected for anisotropy.
26) Band: categorization of measurement into band-1 or band-2. The bands are defined using the average $\phi$ values of Table 2, after Catalogue 1, except for station PSAM (Catalogue 2 only), for which the average value from Table S3 is used.
27) Grade: quality grade (A-D).

## References


6. Kapetanidis, V.; Deschamps, A.; Papadimitriou, P.; Matrullo, E.; Karakonstantis, A.; Bozionelos, G.; Kaviris, G.; Serpetsidaki, A.; Lyon-Caen, H.; Voulgaris, N.; et al. The 2013 earthquake swarm in Helike, Greece: seismic activity at the root of old normal faults. *Geophys. J. Int.* **2015**, *202*, 2044–2073, doi:10.1093/gji/ggv249.
32. Klein, F.W. User's guide to HYPOINVERSE-2000: a Fortran program to solve for earthquake locations and magnitudes. *U.S. Geol. Surv. Prof. Pap.* **2002**, *rep. 02-17*, 1–123.
35. Kapetanidis, V. *Spatiotemporal patterns of microseismicity for the identification of active fault structures using seismic waveform cross-correlation and double-difference relocation*, PhD Thesis, **2017**, Department of Geophysics-Geothermics, Faculty of Geology and Geoenvironment, University of Athens, Greece.
36. Waldhauser, F. hypoDD-A Program to Compute Double-Difference Hypocenter Locations. *U.S. Geol. Surv. Open* File *Rep.* **2001**, *rep. 01*-113, 25 p.
37. Schaff, D.P.; Waldhauser, F. Waveform cross-correlation-based differential travel-time measurements at the northern California seismic network. *Bull. Seismol. Soc. Am.* **2005**, *95*, 2446–2461.
60. Michas, G.; Kapetanidis, V.; Kaviris, G.; Vallianatos, F. Earthquake Diffusion Variations in the Western Gulf of Corinth (Greece). Pure and Applied Geophysics, **2021**. (*in press*)
85. Crampin, S.; Gao, Y.; De Santis, A. A few earthquake conundrums resolved. *J. Asian Earth Sci.* **2013**, *62*, 501–509, doi:10.1016/j.jseaes.2012.10.036.
88. Akazawa, T. A technique for automatic detection of onset time of P and S phases in strong motion records. *Proc. of the 13th World Conf. on Earthquake Engineering, Vancouver, Canada*, **2004**, Paper No. 786.
89. Aki, K.; Richards, P.G. *Quantitative Seismology, 2nd edition*, University Science Books, Sausalito, CA, **2002**.
90. Boatwright, J. Detailed spectral analysis of two small New York State earthquakes. *Bull. Seismol. Soc. Am.* **1978**, *68*, 1117–1131.
91. Boore, D.M.; Boatwright, J. Average body-wave radiation coefficients. *Bull. Seismol. Soc. Am.* **1984**, *74*, 1615–1621.
92. Bowers, D.; Hudson, J.A. Defining the scalar moment of a seismic source with a general moment tensor. *Bull. Seismol. Soc. Am.* **1999**, *89*, 1390–1394.
93. Hanks, T.C.; Kanamori, H. A moment magnitude scale. *J. Geophys. Res. B Solid Earth* **1979**, *84*, 2348–2350, doi:10.1029/JB084iB05p02348.
94. Kapetanidis, V.; Papadimitriou, P. Estimation of arrival-times in intense seismic sequences using a Master-Events methodology based on waveform similarity. *Geophys. J. Int.* **2011**, *187*, 889–917, doi:10.1111/j.1365-246X.2011.05178.x
95. Kapetanidis, V.; Karakonstantis, A.; Papadimitriou, P.; Pavlou, K.; Spingos, I.; Kaviris, G.; Voulgaris, N. The 19 July 2019 earthquake in Athens, Greece: A delayed major aftershock of the 1999 Mw = 6.0 event, or the activation of a different structure? *J. Geodyn.* **2020**, *139*, 101766, doi:10.1016/j.jog.2020.101766.
96. Maeda, N. A method for reading and checking phase times in autoprocessing system of seismic wave data, Zisin. *J. Seismol. Soc. Jpn.* **1985**, 38, 365–379.